University of Southern Queensland

Faculty of Health, Engineering and Sciences

The Effects of Three Phase Asymmetry on Transmission Line Travelling Waves

A dissertation submitted by

Rory Taylor

in fulfillment of the requirements of

ENG4111 and 4112 Research Project

towards the degree of

Bachelor of Engineering (Honours) (Electrical)

Submitted October, 2023

ABSTRACT

The effect of transmission line asymmetry on travelling wave propagation velocity was investigated, for the potential to improve fault location accuracy. It was an analytical and simulation-based investigation using the SimPowerSystem application in the Simulink/MATLAB software. Three-phase asymmetric and symmetric models were constructed from derived 3x3 inductance and capacitance matrices, with each phase represented as a standard ideal two-wire circuit. A modified Clarke matrix transformation was used to decouple the asymmetric system for modal velocity calculations.

The models produced a slight overestimation error, with the ideal symmetric velocity being 1.1% above the ideal upper limit of light speed. Any differences observed in aerial mode propagation velocities between the symmetric and asymmetric models were within this inherent model error. The difference in ground mode velocity was outside the error margin, however, it was found to be caused by the much larger earth-return distance in the asymmetric model, which is not a factor of symmetry. It was therefore concluded that asymmetry has no effect on travelling wave propagation velocity.

The model error was investigated, which increased massively when conductor separation distances were reduced to near conductor radius distances (i.e., close to touching). The radius distance appeared to be a focal point of error, which led to suspected problematic assumptions of the model derivations. Specifically, the inductance and capacitance equations don't actually use the same conductor radius, because the inductance equations account for internal fields, but the capacitance ones don't. Also, the internal inductance equation doesn't account for frequency, therefore neglecting both skin effect and proximity effect. It is suggested these issues be addressed to improve the model for use in further investigations.

University of Southern Queensland

Faculty of Health, Engineering and Sciences

ENG4111 & ENG4112 Research Project

LIMITATIONS OF USE

The Council of the University of Southern Queensland, its Faculty of Health, Engineering and Sciences, and the staff of the University of Southern Queensland, do not accept any responsibility for the truth, accuracy or completeness of material contained within or associated with this dissertation.

Persons using all or any part of this material do so at their own risk, and not at the risk of the Council of the University of Southern Queensland, its Faculty of Health, Engineering and Sciences or the staff of the University of Southern Queensland.

This dissertation reports an educational exercise and has no purpose or validity beyond this exercise. The sole purpose of the course pair entitles "Research Project" is to contribute to the overall education within the student's chosen degree program. This document, the associated hardware, software, drawings, and any other material set out in the associated appendices should not be used for any other purpose: if they are so used, it is entirely at the risk of the user.

CERTIFICATION

I certify that the ideas, designs and experimental work, results, analyses and conclusions set out in this dissertation are entirely my own effort, except where otherwise indicated and acknowledged.

I further certify that the work is original and has not been previously submitted for assessment in any other course or institution, except where specifically stated.

Rory Taylor

Student Number: [redacted]

ACKNOWLEDGEMENTS

I would like to first and foremost thank my wife, Christine, for taking the entire burden of running the household and keeping the family surviving and thriving. Without her endless support, my thesis and studies in general would not have been possible.

I would like to thank my supervisor, Associate Professor Tony Ahfock, for his continued support, teaching, and direction over the course of the research. Our weekly meetings were a great educational experience and crucial to the direction and understanding of the project.

I would also like to thank my parents, Ann and Stan, and mother-in-law, Kerry, who've contributed so much with babysitting and help around the house. Lastly, I'd like to thank my darling children, Aiden and Clara. They are the motivation for all of it.

TABLE OF CONTENTS

LIST OF FIGURES

LIST OF TABLES

CHAPTER 1

INTRODUCTION

1.1 Background

Travelling waves are used to locate transmission line faults. Improving our understanding of transmission line 3-phase asymmetry effects on travelling waves may improve fault location accuracy. This in turn leads to less down time of faulted sections of electricity supply. This represents a reduction of inconvenient 'blackout' time for consumers and a reduction of costs. It also provides more reliability for correctly identifying the faulted component, which otherwise would lead to repeating faults on the same line, further damaging hardware due to stresses created by fault currents (ENTSO-E 2021).

Another benefit of improving speed and/or accuracy of fault detection is to eventually enable the ability to de-energise a broken line section before the live cable even hits the ground. This represents a profound safety enhancement in power distribution. For example, when a car crashes into a pole or a clamp breaks in an urban area, live cables can drop to the ground, risking direct contact with people. Equipment manufacturers have been working towards this rapid fault detection and de-energisation ability for decades, with some technology in trial phase (O'Brien et al. 2016; O'brien & Udren 2018), and the present study may contribute.

Travelling wave-based fault location is the modern standard. Traditional impedance-based methods for fault location involved an error somewhere between 1 – 2 % (Krzysztof, Kowalik & Rasolomampionona 2011; Das et al. 2014; Guzmán et al. 2018) for two-ended detection systems. For example, on a 100 km line, a repair crew would be given an approximate location range of up to 1 - 2 km along which to search for the fault. Considering this may be at night, in bad weather or difficult terrain, this could take considerable time. Single-ended detection systems are much worse, typically ±5% (Krzysztof, Kowalik & Rasolomampionona 2011). The use of travelling waves for locating faults presents a much more accurate method. This technology has been developing over the last couple of decades with the advancement of both sampling rates and time synchronisation of detectors (IEEE 2014).

It works as follows - a fault results in a sudden transient condition which sends voltage & current travelling waves out from its location, which propagate along the transmission line at almost the speed of light. Locating the origin of these waves involves equipment that measures the time difference between detection on either side (or between incident and reflected waves on the one side). Considering

that a wave travels nearly 300 km in a millisecond, the detection precision required for an accurate prediction of origin is only relatively recently achievable. Sampling rates and time synchronisation is now capable of sub-microsecond precision (IEEE 2014; Guzmán et al. 2018). For example, a sampling interval of 1 μs equates to a fault location range within 300 m. Now, fault location accuracy is no longer mostly inhibited by the inherent error presented by the detection instruments, but errors in line length and accuracy of propagation speed along the transmission lines. Therefore, the propagation velocity of the wave is a critical parameter in calculating fault location (Krzysztof, Kowalik & Rasolomampionona 2011), and generally calculated as follows:

$$v_p = \frac{\omega}{\beta} \quad (1)$$

The above propagation velocity (v_p) is proportional to frequency (ω) and dictated by inductance and capacitance only (β). Therefore, this equation only applies to lossless (no resistance value) and balanced systems (Mamiş & Nacaroğlu 2002). Losses are disregarded because travelling waves are generally high frequency, where the frequency-dependent inductive reactance ($X_L = \omega L$) and admittance ($Y = \omega C$) are so much greater than resistance (R) and conductance (G) (Stevenson Jr & Grainger 1994).

1.2 The Problem

The asymmetric placement of conductors in three-phase transmission lines represents a different system inductance and capacitance than the ideal symmetric one to which Equation 1 applies.

First, consider an ideal 3-phase transmission line and how it works: There are 3 conductors (wires) running between towers. Assuming a balanced load, each of them conducts equal alternating current, 120° out of phase with each other. The *sum* of the instantaneous currents anywhere along the combined waveform is zero. This represents perfect balance, which would exist in a physically symmetric arrangements as per Figure 1 below:

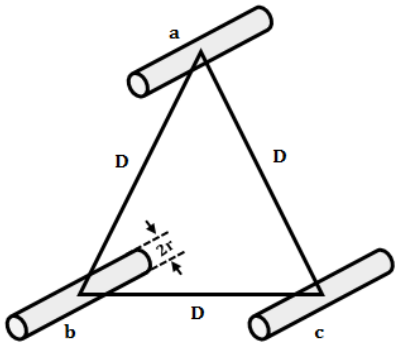

Figure 1. Physically symmetric arrangement of 3-phase transmission line, where the distance (D) is equal between all three phases. Source: https://www.electricaldeck.com/2021/07/inductance-of-transmission-line.html

The flow of current through each line results in flux fields around them. These fields from each phase affect each other's flow of current (mutual capacitance and inductance). In the symmetric arrangement, this is balanced, so the net current of the 3-phases remains zero.

This symmetry also largely negates the effect of the earth flux linkage, because in a balanced system the flux largely cancels out in a similar fashion as the sum of instantaneous currents (but not completely because the conductors have physical separation and do not occupy the same space). The resulting efficiency is what makes 3-phase the most common way electrical grids transfer power. However, a typical overhead power line has its conductors in a straight line across:

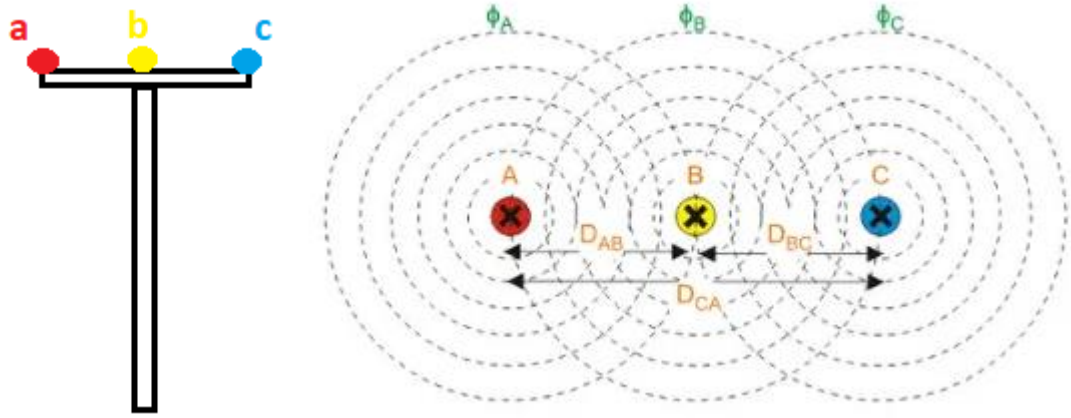

Figure 2. Typical 11 kV transmission line pole (left), showing asymmetric placing of conductors (right – image source: https://www.electrical4u.com/inductance-in-power-transmission-line/).

As displayed in Figure 2 above, the phase '*b'* conductor is exposed to a very different flux field distribution than the phase '*a'* and '*c'* conductors. This imbalance reduces flux cancellation. Therefore, more flux exists resulting in more impedance. Therefore, the currents themselves are unbalanced, forcing a net current flow which involves an earth-return path. That's why there is often line transposition, where the phases are swapped around at each tower to achieve an overall average that balances their impedances:

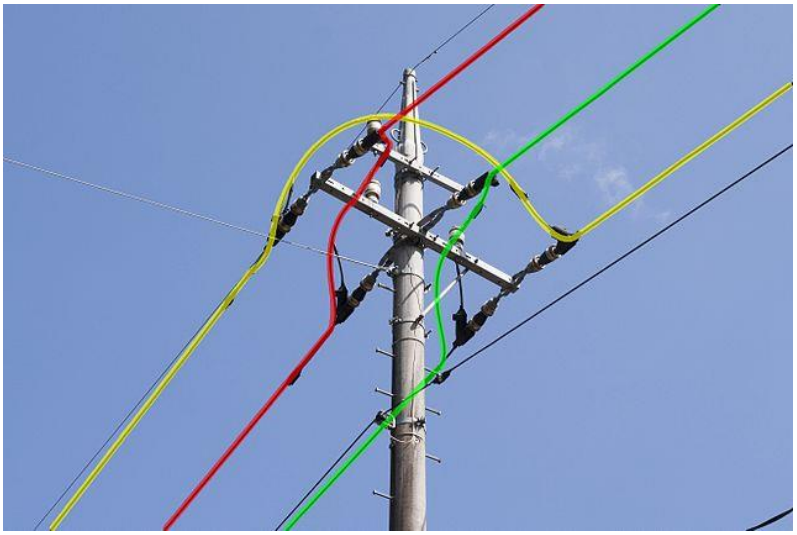

Figure 3. An example of line transposition at a pole. The three line phases are each represented by a different colour. Source: https://commons.wikimedia.org/wiki/File:6.6kV_Power_Line_(Ibaraki,Japan)_02-2.jpg

Many lines are not transposed, and those that are may only approach ideal theoretical balance. Accurate modelling requires accounting for the influence of the imperfect earth-return path (Kaloudas, Papadopoulos & Papagiannis 2008). The extra inductance and mutual inductance with the earth caused by asymmetry is a critical factor in determining the speed of travelling waves.

Power distribution utilities make a direct measurement of the propagation velocity of a given line, with which to calibrate the fault locator (Schweitzer et al. 2014). They use a 'line energisation test', in which usually a circuit breaker is closed at the fault locator at the line origin, and the resultant travelling wave and returned reflection is timed over the known line length. However, there are accuracy issues. For example, the travelling wave velocity fluctuates with external factors such as temperature, dirt, ice (Krzysztof, Kowalik & Rasolomampionona 2011) and humidity (Zhou et al. 2021). Therefore, the development of analytical approaches, such as the present study, are justified.

1.3 Aims and Objectives

The aim of this study was to investigate the effects of 3-phase asymmetrical transmission line arrangement on travelling wave propagation velocity. This was achieved through the following objectives:

1. Research travelling wave and transmission line mathematical theory.
2. Derive mathematical models of travelling waves that incorporates asymmetry-related transmission line effects.
3. Incorporate asymmetry into Simscape transmission line models.
4. Compare and discuss implications of model outcomes for protection systems based on travelling waves.

1.4 Thesis Structure

Chapter 2 is the review of the literature primarily for analytical studies, as well as the relevant numerical studies.

Chapter 3 is the methodology. Firstly, the mathematics of travelling waves were explored, then the asymmetric and symmetric 3-phase models were derived. The simulation testing proceeded stepwise in complexity, beginning with classical single-phase transmission lines as a proof of concept. Once the model was behaving on the simulator as mathematically expected, then the testing of the derived 3-phase models could proceed.

Chapter 4 is the results and discussion, which is presented as a two-fold exploration – simulation and analytical, which are generally correlated at each step of investigation. Any evidence that emerged of different travelling wave propagation speeds between models was explored further in relation to measurement and inherent model error, as well as comparability between models.

Chapter 5 is the conclusion, in which any evidence of effects of asymmetry on propagation velocity was ultimately weighed against inherent model error and model comparability.

CHAPTER 2

LITERATURE REVIEW

Analytical studies of the effects of asymmetry on travelling waves are relatively scarce in the literature. Transient analysis tends to be done by numerical approach, with commercial simulation tools that can handle large and complex power networks (Bellan & Superti-Furga 2018).

2.1 Analytical Studies

An example for a balanced 3-phase line is reported (de Magalhães Júnior & Lopes 2021), using the Clarke transformation to develop mathematical expressions as functions of line and fault parameters. They also noted that other transformation matrices, such as the Karrenbauer and Wedepohl would also have been appropriate. Importantly, they included losses in their simulated lines (Bergeron and JMarti lossy line models). Comparing their mathematical results with the simulations, they found their formulas reliable for aerial travelling waves, but less so for ground mode, concluding that different tower geometries and ground characteristics have different effects on travelling waves.

The following literature reports improved modelling accuracy of asymmetric 3-phase systems by modifications of traditional transformation matrices, focussing mainly on Clarke matrix modifications. An example of an analytical approach (Bellan 2019, 2020) uses a modified Clarke transformation to derive more appropriate circuit models for transients in asymmetric 3-phase systems. These equivalent circuits model single- or double-line switching (asymmetric transients occurring when not all three phases are involved in switching events). Firstly, the switching section is ‘removed’, leaving a balanced 3-phase system. Then the Clarke transformation is applied and the three Thevenin equivalents (open circuit voltage and equivalent impedance) in the mode domain can be derived. Secondly, the line-switching voltage and current constraints are transformed, and the resulting modal constraints are implemented in the modal Thevenin equivalents.

2.2 Numerical Studies

The literature for numerical studies of transmission line travelling waves is extensive. The following review is narrowed to studies involving asymmetry and modified modal transformation techniques.

Authors (Pang et al. 2019) investigated travelling waves on a typical 3-phase asymmetric 110 kV transmission line. They calculated the line parameters then derived a decoupling algorithm based on a modified Karenbauer transformation, in which the decoupled coupling components accounted for only 2 %, which was better than their Clarke matrix transform. They also found that the travelling waves attenuate with distance, in manner that's proportional to their frequencies, and travelling waves usually occur at high frequencies in the kHz to MHz range (de Magalhães Júnior & Lopes 2021). Another study utilised the Karrenbauer transform (Liang et al. 2017) to decouple and analyse ground-mode travelling wave characteristics to investigate the relationship between ground-mode propagation velocity of travelling waves and fault distance. This was used to propose a grounding fault-location method.

Another fault location method involved untransposed lines decoupled using an eigenvalue decomposition technique (Lu et al. 2020; Lu et al. 2021). This is followed with the Bergeron method, in which the distributed line inductances and capacitances, and the lumped line resistances, are factored to solve the voltage distribution of the line.

Another approach, the 'zeroth-order' modal solution, has been a common approximation method (Faria & Mendez 1997). This is where the average of the main diagonal is taken, and the average of the off-diagonals are taken. An approximation matrix is reconstructed using these averages, which will be a balanced matrix (since all off-diagonals are now equal). Now, transforming this yields a diagonal eigenvalue matrix, used to obtain fairly accurate results at least for non-transposed bilateral lines (Faria & Mendez 1997). This zeroth-order method will also be employed in the present study.

This method has been built upon with the addition of a perturbation theory approach to obtain a first-order approximation (Faria & Briceno 1997; Faria & Mendez 1997; Faria 2000). It is a numerical iterative approach, with the quasi-modes represented as the above approximations plus a perturbation. It forms the basis of several studies (Prado et al. 2010; Da Costa et al. 2011; Prado et al. 2011; Prado et al. 2012), where the off-diagonal elements are represented as relative values. A corrector matrix works to continuously 'tune' the modified Clarke transformation matrix with correction terms (perturbations) to reduce the relative error between quasi-mode and exact values.

2.3 Summary

Analytical studies of asymmetry-related transmission line effects are a minority in the literature compared to the plethora of numerical studies. Those analytical studies reviewed are supported by detailed background theory to support their model constructions. Several transformation matrix methods (Clarke, Wedepohl etc) are employed and necessarily altered to apply to otherwise problematic asymmetric lines.

Such models would then be simulated, for example, with Matlab's Simulink or Alternative Transients Program (ATP). After verification through comparison with known theory or real-world data, they would be used to investigate various hypotheses. The outcomes of which are usually discussed in the context of their potential benefits to fault location technology. For example, some have application for improving location accuracy, or others for improving real-world reliability of correct peak detection, because currently significant detection problems are caused by lots of reflections from lots of poles and branches. The present study uses some theory from the review, such as the zeroth order Clarke matrix modification, to investigate the effects of asymmetry on travelling wave propagation velocity. The implications of which are targeted at improving fault location device accuracy.

CHAPTER 3

METHODOLOGY

This project was an analytical and simulation-based investigation. The goal was to establish if asymmetry affects the travelling waves propagation velocity. Firstly, the mathematics of travelling waves and transmission lines needed to be explored in order to create a model for simulation. The simulation testing needed to begin simple and correlate with classical theory to confirm it was being operated correctly. Then the testing of the derived models could proceed.

The SimPowerSystem, an application in the Simulink/MATLAB software, was the simulation tool used. It uses the Bergeron method mentioned in the literature review for the transmission line model.

3.1 Mathematical Background of Travelling Waves

Travelling waves are both time- and space-dependent, and are mathematically defined by the partial differential equations (known as the Telegrapher's Equations):

$$\frac{\partial^2 V(x,s)}{\partial x^2} = Z \cdot Y \cdot V(x,s)$$

$$\frac{\partial^2 I(x,s)}{\partial x^2} = Z \cdot Y \cdot I(x,s)$$

The above voltage and current transmission line equations are derived from a distributed parameter transmission line equivalent circuit, where 'Z' and 'Y' represent series impedance and shunt admittance per unit length respectively, and 'x' represents the longitudinal coordinate.

To solve the travelling wave equations for a given 3-phase line, tools such as the Clarke transformation have been used extensively. It is a modal transformation matrix, where all electrical parameters and line representative matrices are obtained in mode domain (Prado et al. 2011). Modal signals are basically distortion-free constant frequency signals (Hedman 1965). This domain simplifies things, because the representative impedance matrices of the line are diagonalised and the frequency influence can be analysed independently for every mode. This means that they can be modelled as 3 single-phase lines, because the transformation removes the mutual terms of the impedance and admittance matrices (Carvalho et al. 2016).

The travelling waves propagate from a fault location in both directions, and their velocity depends on the mode ('α', 'β' or '0'). The modal decoupling technique using the Clarke matrix for standard symmetric systems is as follows: The line has a per-unit length series impedance matrix (Z) and per-unit length shunt admittance matrix (Y). For instance, the impedances represented in Z are composed of frequency-dependent resistances and inductances of the general form $Z_{ij} = R_{ij} + j\omega L_{ij}$, and represented in matrix form (The admittance (Y) matrix is represented in the same way, with $Y_{ij} = G_{ij} + j\omega C_{ij}$):

$$Z = \begin{bmatrix} Z_{11} & Z_{12} & Z_{13} \\ Z_{21} & Z_{22} & Z_{23} \\ Z_{31} & Z_{32} & Z_{33} \end{bmatrix} \qquad Y = \begin{bmatrix} Y_{11} & Y_{12} & Y_{13} \\ Y_{21} & Y_{22} & Y_{23} \\ Y_{31} & Y_{32} & Y_{33} \end{bmatrix}$$

Looking at the subscripts of the elements, the main diagonal impedances are independent, consisting of parameters of the three single phases on their own (self-impedances). The off-diagonal elements consist of mutual impedances between phases. Also recall that the system is symmetric, so all the main diagonal elements are equal, and all the mutual couplings (off-diagonal elements) are equal. Therefore, this balanced system would be of the form:

$$[ZY]_{bal} = \begin{bmatrix} h & m & m \\ m & h & m \\ m & m & h \end{bmatrix} \qquad (2)$$

To decouple this system, the mutual impedances are removed via the Clarke transformation matrix shown below:

$$T_{CL} = \sqrt{\frac{2}{3}} \begin{bmatrix} 1 & -\frac{1}{2} & -\frac{1}{2} \\ 0 & \frac{\sqrt{3}}{2} & -\frac{\sqrt{3}}{2} \\ \frac{1}{\sqrt{2}} & \frac{1}{\sqrt{2}} & \frac{1}{\sqrt{2}} \end{bmatrix}$$

Note that this is an orthogonal matrix, so T-inverse (T^{-1}) = T-transpose (T^{T}).

Applying the transform yields the decoupled system eigenvalues:

$$T \cdot Z \cdot Y \cdot T^{-1} = \begin{bmatrix} \lambda_\alpha & 0 & 0 \\ 0 & \lambda_\beta & 0 \\ 0 & 0 & \lambda_0 \end{bmatrix}$$ where λ is an eigenvalue and α, β and 0 are the modes.

For a balanced system, $\lambda_\alpha = \lambda_\beta = (h - m)$ and $\lambda_0 = (h + 2m)$. The modes 'α' and 'β' are also referred to as the arial modes, and '0' is the ground mode. Each mode has a different propagation velocity and impedance, with the ground mode being the slowest and most variable (Ancell & Pahalawaththa 1994).

However, it is problematic applying the Clarke transformation to asymmetric 3-phase systems (Da Costa et al. 2011; Prado et al. 2011; Bellan 2020; Lu et al. 2021). Only lossless balanced systems can be accurately solved analytically (Faria & Briceno 1997; Mamiş & Nacaroğlu 2002). When eigenvector matrices are transformed, the resultant matrix is not diagonal, meaning the above zero values outside of the main diagonal turn out to be non-zero values, and this is referred to as a 'quasi-mode' matrix. These elements are not negligible when compared with the eigenvalues and represent problematic couplings between these modes. Therefore, researchers tackling the asymmetry problem generally do so by modifying the Clarke transformation.

3.2 Modified Clarke Transformation

In contrast to $[ZY]_{bal}$ (2), for an unbalanced system, but assuming the asymmetric conductor arrangement has at least bilateral symmetry (see Figure 2, where a line of symmetry bisects vertically through conductor *b*), the matrix would be of the form:

$$Z \text{ and } Y = \begin{bmatrix} a & c & d \\ c & b & c \\ d & c & a \end{bmatrix} \qquad [ZY] = \begin{bmatrix} x & y & z \\ w & u & w \\ z & y & x \end{bmatrix}$$ (Faria & Mendez 1997)

To obtain the $[ZY]_{bal}$, a common averaging technique is used, introduced in the literature review (Faria & Mendez 1997). The main diagonal elements are replaced by their average ($h = \frac{x+u+x}{3}$), and the off-diagonal elements are replaced by their average ($m = \frac{w+y+z}{3}$), which therefore converts the matrix

back to the balanced form shown in (2). This is known as a zeroth-order approximation matrix. This mathematical averaging process is possibly akin to physical line transposition.

3.3 Initial Single Phase Simulator Test Circuit

The testing began with a preliminary single-phase DC investigation of travelling wave velocity in a classical two-wire circuit. Figure 4 displays the Simulink construct, where a switch sends a step input of magnitude 100 A along a transmission line. Each distributed parameters line section (upper blank rectangles in series) is 200 km long, with the entire line (800 km) being terminated by a very high resistance (~open circuit). Whilst voltage scopes were placed between each line section, only the one at the start of the line (V5) was reported on, being the likely location of a detection device.

A second switch connected at the middle of the line functions as a fault. This was included once the initial testing of the DC wave propagation was completed, with the source also then being changed to AC.

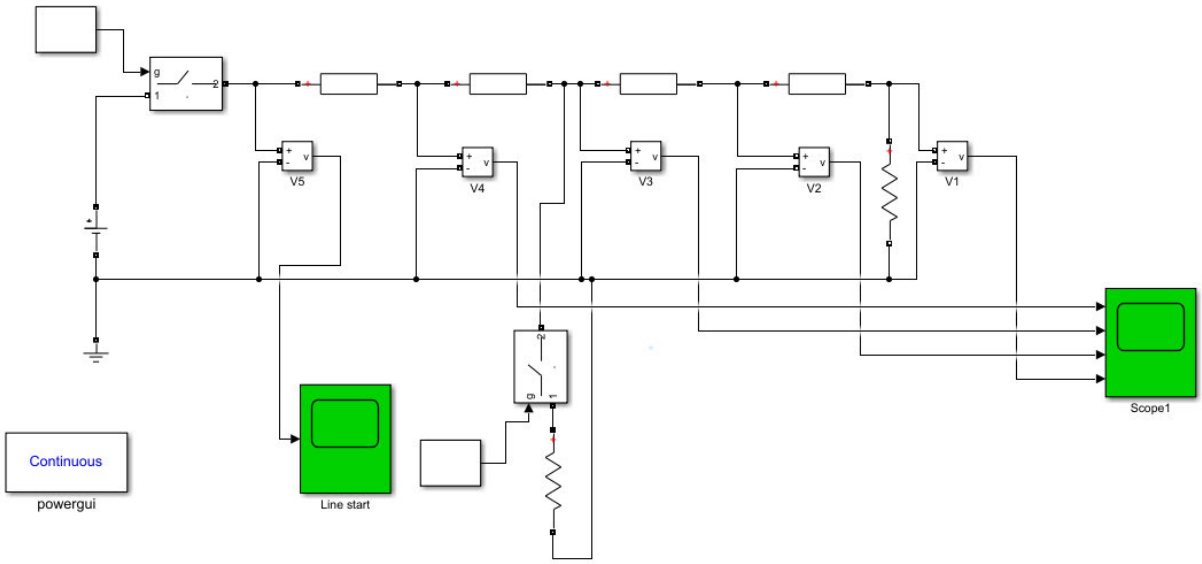

Figure 4. Single-phase transmission line with fault model. The L and C values previous were entered into the distributed parameters line sections (200 km long each).

3.4 3-Phase Simulator Circuit:

The main parameters involved in constructing the models are the inductance (L) and capacitance (C) matrices. The 3-phase model is built from a 3x3 matrix of each, with each phase represented as a standard two-wire circuit. These parameters depend on the geometric placement of the conductors. The default tower geometry was taken from the Simulink 'Line Parameter Calculator' application for an

example 25 kV three-phase line. The conductors were 10.37 m high (not including line sag between poles) and the outer conductors being 1.24 m out on each side.

The 3-phase circuit (Figure 5) was of similar structure as the single phase. An alpha-beta-zero transform block (Clarke transformation) was also included on the scope. Incident and reflected wave time intervals were measured 'manually' by lining up the measuring cursors on the scope with the first discernable peaks of each wave group. Both voltage and current scopes were included in the model, but only the voltage signal was reported on due to its much more definable peaks. The 3-phase fault block in the center of the lines was customizable to allow different types of faults (Figure 6), for example line-to-line, or line-to-ground.

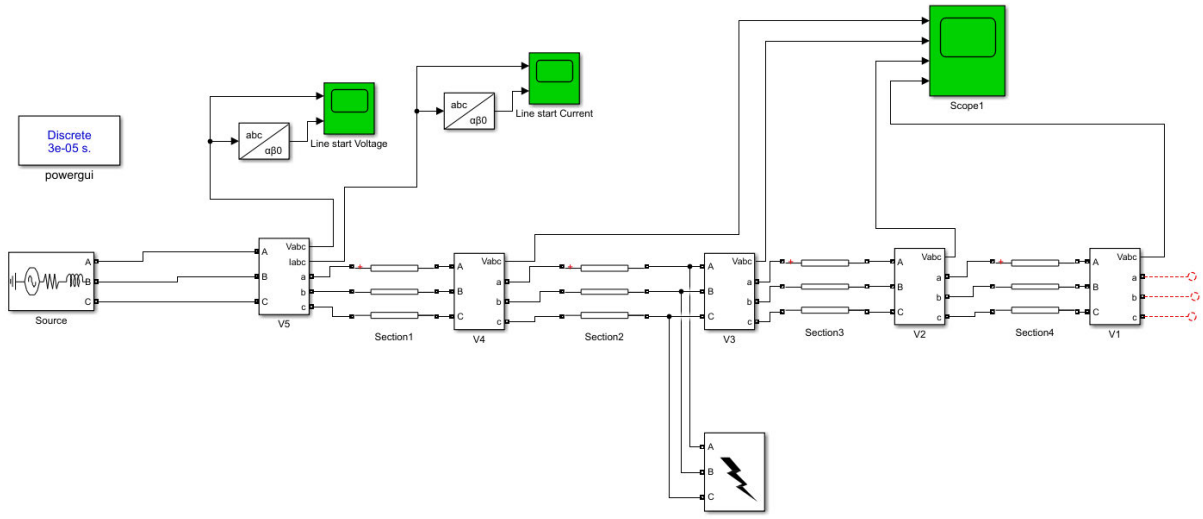

Figure 5. Simscape model layout. The L and C matrices derived in the methodology section were entered into the distributed parameters 3-phase line sections. Both voltage and current traces were observed, with the former only being used for measurements due to peak clarity. The αβ0 transformation blocks were also a tool to improve clarity for measurements.

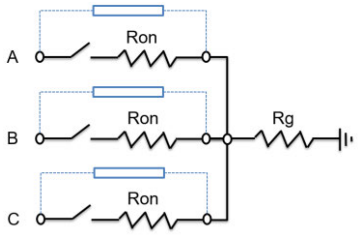

Figure 6. Three-phase fault block. It is implemented as a 3-phase circuit breaker with the phases able to be individually closed/open. The ground connection can also be opened for non-ground faults.

3.5 Inductance Matrix of the Transmission Line

To create a simulation model, it was necessary to construct the 3x3 inductance matrix. The three elements of the main diagonal represent the self-inductances of each phase. The remaining six off-diagonal components represent the mutual inductances between phases.

There are different ways of constructing the balanced symmetric model, but the asymmetric conductor arrangement is unbalanced ($I_a + I_b + I_c \neq 0$). Therefore, the three-phase system was treated as three separate two-wire circuits – each phase conductor with its earth-return (designated conductor 'p'). It is important to note here that the earth-return path was modelled as a second identical conductor, for simplicity purposes. A real earth-return path obviously has different and non-homogenous material properties (Chalangar et al. 2019).

The self-inductances were calculated directly with standard equations for a two-wire circuit:

Flux density standard equation for a single conductor:

$$B = \frac{\mu_0 I}{2\pi x} \qquad (3)$$

where x = distance from conductor (*Note: designated 'z', not 'x', in Figure 7); and

μ_0 = permeability of free space (= 4π x 10^{-7})

Integrating this to find flux linkage standard equation:

$$\Psi_{ext} = \frac{\mu_0 I}{2\pi} \int_r^D \frac{1}{x}\, dx \qquad \text{(external flux linkage of single conductor)}$$

$$\Psi_{int} = \frac{\mu_0 I}{2\pi} \int_0^r \frac{x^3}{r^4}\, dx \qquad \text{(internal flux linkage of single conductor)}$$

$$\Psi = \frac{\mu_0 I}{\pi} \cdot \ln\left(\frac{D}{r'}\right) \qquad \text{(Total flux linkage of both conductors in circuit)} \qquad (4)$$

where D = distance between conductors; and

r' = conductor equivalent radius = 0.7788r

This leads to the self-inductance standard equation:

$$L_{self} = 4x10^{-7}\left(\ln\left(\frac{D}{r'}\right)\right) \qquad (5)$$

To calculate the mutual inductance elements, the total flux density of one circuit where it crosses the other circuit was required. In other words, to integrate the flux density of one circuit along the line integral represented by the other circuit.

Breaking this problem down, superposition was used to sum the flux densities of each conductor of one circuit where they 'cross' the other circuit. The flux densities are vectors - they have both magnitude and direction, so the following needed consideration:

- Their magnitude is a function of distance from their source conductor – equation (3).
- The superposition of the two flux lines from conductors 'a' and 'p' across circuit b-p is a function of their intersecting angle.

3.5.1 Asymmetric Arrangement

Although there are 6 elements, they are represented by only 3 different arrangements:

1. Flux linkage from the current in circuit a-p with circuit b-p (Figure 7). This will lead to both L_{ab} and L_{cb} since they are geometrically identical arrangements.
2. Flux linkage from the current in circuit b-p with circuit a-p (Figure 8). Geometrically identical to both L_{ba} and L_{bc}.
3. Flux linkage from the current in circuit a-p with circuit c-p (Figure 10). Geometrically identical to both L_{ac} and L_{ca}.

3.5.1.1 *Flux linkage from the current in circuit a-p with circuit b-p.*

Circuit a-p consists of the current flowing in conductor ‘a’ and its earth-return equivalent ‘p’.

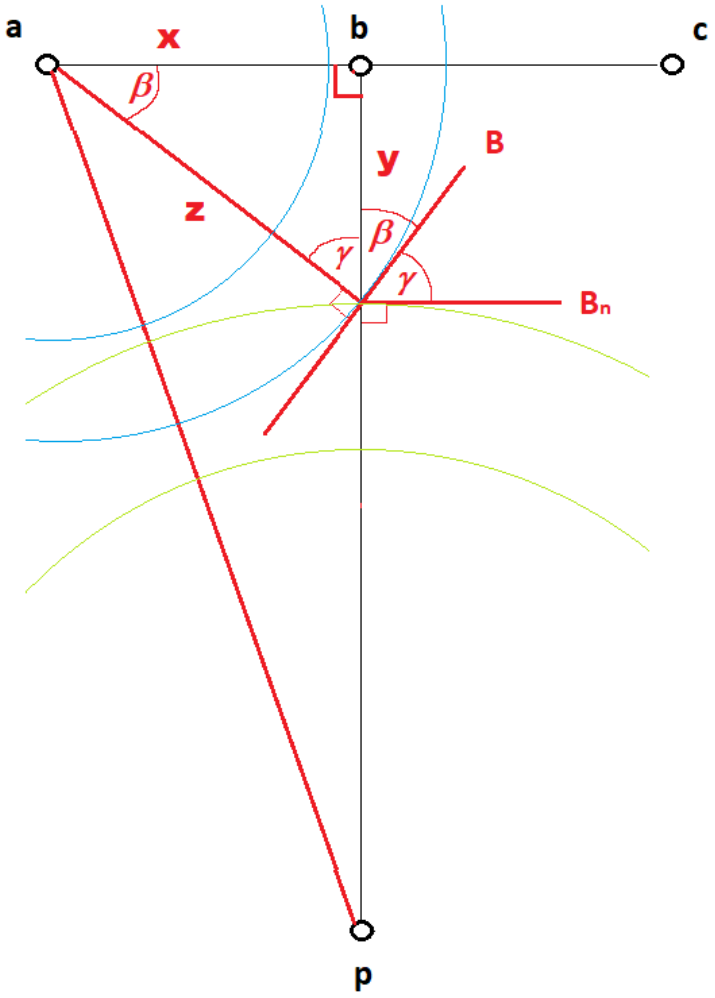

Figure 7. Geometry of the tower conductor arrangement, showing the three phases at the top, and an earth-return (‘p’) at the bottom. The circular lines represent flux direction from conductor ‘a’ (blue) and ‘p’ (green). The angle at which they cross the normal (‘Bn’) to circuit b-p is designated ‘γ’.

The summation of the flux densities from the two conductors ‘a’ and ‘p’ is at maximum when they are parallel (0° intersection). However, they are never parallel along line b-p. From inspection of Figure 7, their intersecting angle gradually decreases from perpendicular at the ‘b’ end, to almost parallel at the ‘p’ end. We need to define this intersection angle as a function of distance along line b-p.

The position of conductor ‘p’ simplifies things because it is a common point of both circuits. Therefore, the angle of ‘p’ conductor flux density is a constant 90° to the circuit b-p, representing the normal (Bn) to line b-p, and the reference direction. Hence, the angle of ‘a’ conductor flux intersecting ‘p’ conductor flux along circuit b-p is the same as the intersecting angle of ‘a’ conductor flux with ‘Bn’.

The standard equations apply directly to conductor ‘p’ (since its flux density is always normal to the line integral b-p and is the constant reference 0° for conductor ‘a’ flux intersection).

The standard equation (4) includes both wires, so it must include a factor of ½ to apply to conductor ‘p’ alone. It also uses the equivalent radius (r’) to simplify internal plus external inductances, but it was converted back to standard radius (r) because it made the Ψ_{pb} equation more compatible with the Ψ_{ab} equation (evident later), which is external flux linkage only:

$$r' = 0.7788r = r \cdot e^{-\frac{1}{4}}$$

$$\Psi_{pb} = \frac{\mu_0 I_a}{2\pi} \cdot \ln\left(\frac{D}{r \cdot e^{-\frac{1}{4}}}\right)$$

$$\Psi_{pb} = \frac{\mu_0 I_a}{2\pi} \cdot \ln\left(\frac{D \cdot e^{\frac{1}{4}}}{r}\right)$$

$$\Psi_{pb} = \frac{\mu_0 I_a}{2\pi} \cdot \left(\ln e^{\frac{1}{4}} + \ln\left(\frac{D}{r}\right)\right)$$

$$\Psi_{pb} = \frac{\mu_0 I_a}{2\pi} \cdot \left(\frac{1}{4} + \ln\left(\frac{D}{r}\right)\right)$$

Therefore, that the external only flux linkage of the above is:

$$\Psi_{pb\_ext} = \frac{\mu_0 I_a}{2\pi} \cdot \left(\ln\left(\frac{D}{r}\right)\right) \qquad (6)$$

So far, there’s the standard equations for flux density (3) and flux linkage from the ‘p’ conductor with circuit b-p (6). Next, to derive the flux density from conductor ‘a’ across line b-p, these equations need to be modified using Figure 7 and trigonometry.

Firstly, the derivation the magnitude of the flux density from conductor ‘a’ as a function of distance along line b-p:

Starting with the standard equation (3) applied to Figure 7:

$$B = \frac{\mu_0 I_a}{2\pi z} \qquad (7)$$

where z = distance from conductor ‘a’.

However, since integration was along line b-p and not line a-p, the variable ‘z’ was needed to be defined as a function of line integral variable ‘y’:

$$z^2 = x^2 + y^2$$

$$z = \sqrt{x^2 + y^2} \qquad (8)$$

In this case, ‘x’ is a constant, the distance between conductors ‘a’ and ‘b’. Substituting (8) back into the original equation (7):

$$B = \frac{\mu_0 I_a}{2\pi\sqrt{x^2 + y^2}}$$

This is the magnitude. The angle must also be incorporated, which is the component of B that is normal to the line b-p:

$$Bn = \frac{\mu_0 I_a \cdot cos(\gamma)}{2\pi\sqrt{x^2 + y^2}} \qquad (9)$$

As discussed previously, the angle ‘γ’ is also a variable and a function of ‘y’, so needed to be defined as such:

$$cos(\gamma) = \frac{y}{z} \qquad (10)$$

Substituting (8) into (10):

$$cos(\gamma) = \frac{y}{\sqrt{x^2 + y^2}} \qquad (11)$$

Substituting (11) back into (9):

$$Bn = \frac{\mu_0 I_a \cdot y}{2\pi\sqrt{x^2 + y^2}\sqrt{x^2 + y^2}}$$

$$Bn = \frac{\mu_0 I_a \cdot y}{2\pi(x^2 + y^2)}$$

Integrating this along line b-p to find flux linkage:

$$\Psi_{ab} = \frac{\mu_0 I_a}{2\pi} \int_r^D \frac{y}{(x^2 + y^2)}\, dy$$

Using the standard integral: $\int \frac{x dx}{a^2 + x^2} = \frac{1}{2} \ln(a^2 + x^2)$

$$\Psi_{ab} = \frac{\mu_0 I_a}{4\pi} [ln(x^2 + D^2) - ln(x^2 + r^2)]$$

$$\Psi_{ab} = \frac{\mu_0 I_a}{4\pi} \cdot \ln\left(\frac{x^2 + D^2}{x^2 + r^2}\right) \quad (12)$$

Note that the constants 'x' and 'D' represent specific distances as described below equations (4) and (8). These generic notations were kept for simplicity throughout the following workings. However, these notations are also used for the workings through the other arrangements where they represent different specific distances. Therefore, the generic notations 'x' and 'D' were only replaced with their specific distance notations in the final inductance equations.

So far, the equations for flux linkages from conductors 'p' (6) and 'a' (12) with circuit b-p are obtained. These were used to find the mutual inductance from circuit a-p to circuit b-p, representing the inductance matrix element L_{ab}. Using superposition, this element was constructed from the internal and external inductances for conductors 'a' and 'p':

$$L_{ab} = L_{int\,(a)} + L_{int\,(p)} + \left(\frac{\Psi_{ab} + \Psi_{pb\_ext}}{I_a}\right) \quad (13)$$

where $L_{int\,(a)} = L_{int\,(p)} = 0.5 \times 10^{-7}$ H/m (constant)

Substituting in (6) and (12) to (13):

$$L_{ab} = 0.5x10^{-7} + 0.5x10^{-7} + \frac{\mu_0}{4\pi} \cdot \ln\left(\frac{x^2 + D^2}{x^2 + r^2}\right) + \frac{\mu_0}{2\pi} \cdot \left(\ln\left(\frac{D}{r}\right)\right)$$

where $\frac{\mu_0}{4\pi} = 1x10^{-7}$

$$L_{ab} = 1x10^{-7} + 1x10^{-7}\ln\left(\frac{x^2 + D^2}{x^2 + r^2}\right) + 2x10^{-7}\left(\ln\left(\frac{D}{r}\right)\right)$$

$$L_{ab} = 1x10^{-7} + 1x10^{-7}\ln\left(\frac{x^2 + D^2}{x^2 + r^2}\right) + 2x10^{-7}\ln\left(\frac{D}{r}\right)$$

$$L_{ab} = 1x10^{-7} + 1x10^{-7}\left(\ln\left(\frac{x^2 + D^2}{x^2 + r^2}\right) + 2\ln\left(\frac{D}{r}\right)\right)$$

$$L_{ab} = 1x10^{-7}\left(1 + \ln\left(\frac{x^2 + D^2}{x^2 + r^2}\right) + \ln\left(\frac{D}{r}\right)^2\right)$$

$$L_{ab} = 1x10^{-7}\left(1 + \ln\left(\frac{D^2(x^2 + D^2)}{r^2(x^2 + r^2)}\right)\right)$$

This is the equation for the mutual inductance element L_{ab} and its mirror image L_{cb} of the 3x3 inductance matrix. As mentioned previously, the generic notations 'x' and 'D' must now be replaced with their specific distance notations because they are distinct for each section/arrangement. For the current arrangement:

x = distance between conductors 'a' and 'b' = 'D_{ab}'

D = distance between conductors 'b' and 'p' (line integral distance) = 'D_{bp}'

$$L_{ab} = 1x10^{-7}\left(1 + \ln\left(\frac{{D_{bp}}^2({D_{ab}}^2 + {D_{bp}}^2)}{r^2({D_{ab}}^2 + r^2)}\right)\right) \quad (14)$$

3.5.1.2 *Flux linkage from the current in circuit b-p with circuit a-p*

Circuit b-p consists of the current flowing in conductor ‘b’ and its earth-return equivalent ‘p’. We now need to integrate the sum of conductor ‘b’ and ‘p’ flux densities along line a-p. The equations will be derived using Figure 8.

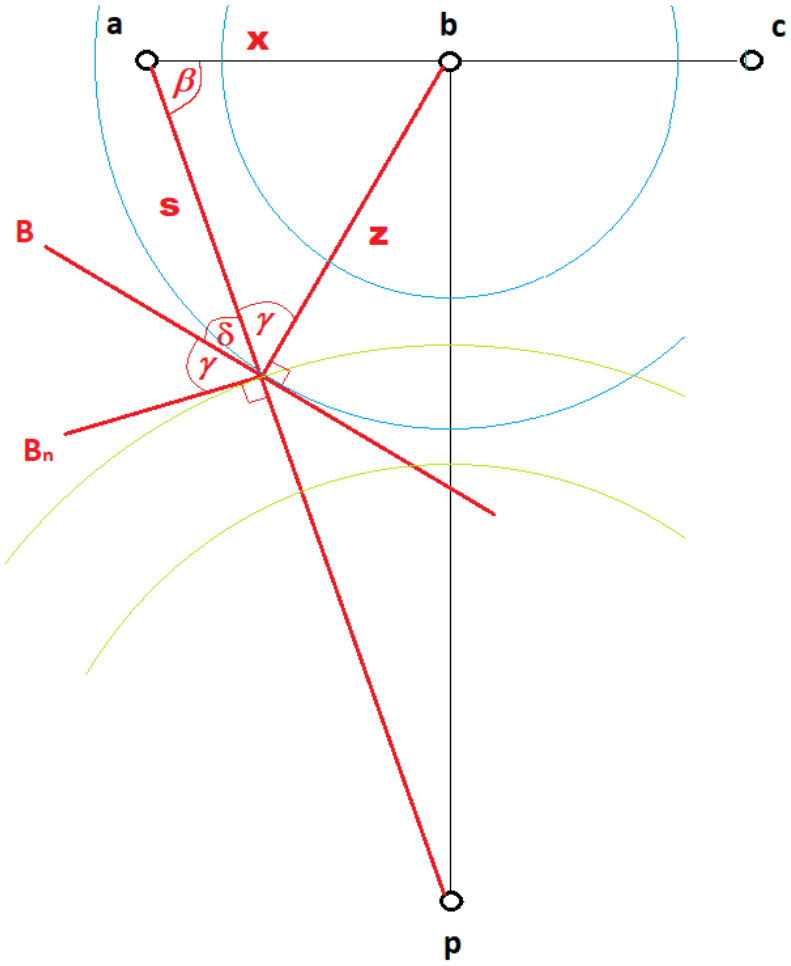

Figure 8. Geometry of the tower conductor arrangement, showing the three phases at the top, and an earth-return (‘p’) at the bottom. The circular lines represent flux direction from conductor ‘b’ (blue) and ‘p’ (green). The angle at which they cross the normal (‘Bn’) to circuit a-p is designated ‘γ’.

The same principle applies as before, in that ‘p’ is a common point to both circuits, a constant 90° to the line integral a-p, and is subject to the standard equations (3) and (4). Therefore, the flux density from conductor ‘b’ relative to the normal of the line integral a-p is required:

$$Bn = \frac{\mu_0 I_b \cdot cos(\gamma)}{2\pi z} \qquad (15)$$

Once again, variables ‘z’ and cos(γ) must be defined as functions of the line integral variable ‘s’. This time however, the trigonometry is a bit different.

Unlike the right triangle (a-b-p) in Figure 7, there exists an obtuse triangle this time. ‘The Cosine Rule’ (16) can be applied:

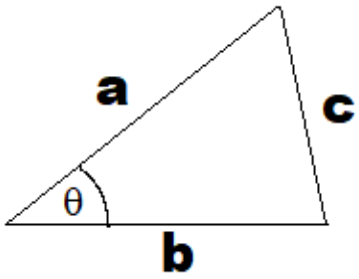

Figure 9. Obtuse triangle for application of the Cosine Rule.

$$\text{Where } c = \sqrt{a^2 + b^2 - 2ab \cdot cos(\theta)} \qquad (16)$$

Applying this rule directly to Figure 8, ‘z’ can be defined as a function of ‘s’:

$$z = \sqrt{s^2 + x^2 - 2xs \cdot cos(\beta)} \qquad (17)$$

where ‘x’ and cos(β) are constants.

Similarly, it is used to define cos(γ) as a function of ‘s’:

$$x = \sqrt{s^2 + z^2 - 2zs \cdot cos(\gamma)}$$

$$x^2 = s^2 + z^2 - 2zs \cdot cos(\gamma)$$

$$2zs \cdot cos(\gamma) = s^2 + z^2 - x^2$$

$$\cos(\gamma) = \frac{s^2+z^2-x^2}{2zs} \qquad (18)$$

Substituting (17) into (18):

$$\cos(\gamma) = \frac{s^2 + (\sqrt{s^2 + x^2 - 2xs \cdot cos(\beta)})^2 - x^2}{2s(\sqrt{s^2 + x^2 - 2xs \cdot cos(\beta)})}$$

$$\cos(\gamma) = \frac{s^2 + (s^2 + x^2 - 2xs \cdot cos(\beta)) - x^2}{2s(\sqrt{s^2 + x^2 - 2xs \cdot cos(\beta)})}$$

$$\cos(\gamma) = \frac{2s^2 - 2xs \cdot cos(\beta)}{2s(\sqrt{s^2 + x^2 - 2xs \cdot cos(\beta)})}$$

$$\cos(\gamma) = \frac{s - x \cdot cos(\beta)}{\sqrt{s^2 - 2xs \cdot cos(\beta) + x^2}} \quad (19)$$

Substituting both (19) and (17) back into (15):

$$Bn = \frac{\mu_0 I_b \cdot (s - x \cdot cos(\beta))}{2\pi\sqrt{s^2 - 2xs \cdot cos(\beta) + x^2}\sqrt{s^2 - 2xs \cdot cos(\beta) + x^2}}$$

$$Bn = \frac{\mu_0 I_b \cdot (s - x \cdot cos(\beta))}{2\pi(s^2 - 2xs \cdot cos(\beta) + x^2)} \quad (20)$$

Now this can be integrated to find the flux linkage along line integral a-p. Since ‘x’ and cos(β) are constants, ‘cos(β)’ will be denoted as ‘a’ for clarity, so (20) condenses to:

$$Bn = \frac{\mu_0 I_b \cdot (s - xa)}{2\pi(s^2 - 2xas + x^2)} \quad (21)$$

To find flux linkage, the integration of (21) will be:

$$\Psi_{ba} = \frac{\mu_0 I_b}{2\pi} \int_r^D \frac{(s - xa)}{(s^2 - 2xas + x^2)}\, ds \quad (22)$$

where D = distance a-p; and

r = conductor radius

This can be integrated by ‘u’-substitution:

Let ‘u’ = integrand denominator: $u = s^2 - 2xas + x^2$ (23)

$$\frac{du}{ds} = 2s - 2xa$$

$$du = (2s - 2xa)ds$$

$$\frac{1}{2}du = (s - xa)ds \quad (24)$$

Substituting (23) and (24) back into (22):

$$\Psi_{ba} = \frac{\mu_0 I_b}{2\pi} \int_r^D \frac{(\frac{1}{2} du)}{u}$$

$$\Psi_{ba} = \frac{\mu_0 I_b}{4\pi} \int_r^D \frac{du}{u}$$

$$\Psi_{ba} = \frac{\mu_0 I_b}{4\pi} \int_r^D \frac{1}{u}\, du$$

Using the standard integral: $\int \frac{1}{x} dx = \ln x$

$$\Psi_{ba} = \frac{\mu_0 I_b}{4\pi} [\ln (u)]_r^D \qquad (25)$$

Substituting back (23) into (25):

$$\Psi_{ba} = \frac{\mu_0 I_b}{4\pi} [\ln (s^2 - 2xas + x^2)]_r^D$$

$$\Psi_{ba} = \frac{\mu_0 I_b}{4\pi} [\ln(D^2 - 2xaD + x^2) - ln(r^2 - 2xar + x^2)]$$

$$\Psi_{ba} = \frac{\mu_0 I_b}{4\pi} \cdot \ln\left(\frac{D^2 - 2xaD + x^2}{r^2 - 2xar + x^2}\right)$$

Substituting back ‘a’ for cos(β):

$$\Psi_{ba} = \frac{\mu_0 I_b}{4\pi} \cdot \ln\left(\frac{D^2 - 2xD \cdot cos(\beta) + x^2}{r^2 - 2xr \cdot cos(\beta) + x^2}\right)$$

Next, the mutual inductance from circuit b-p to circuit a-p is required, representing the inductance matrix element L_{ba}. Similar to (13), this includes the internal and external inductances of conductors ‘b’ and ‘p’:

$$L_{ba} = L_{int\,(b)} + L_{int\,(p)} + \left(\frac{\Psi_{ba} + \Psi_{pa\_ext}}{I_b}\right)$$

where $L_{int\,(b)} = L_{int\,(p)}$ = 0.5 x 10^{-7}

$$L_{ba} = 0.5x10^{-7} + 0.5x10^{-7} + \frac{\mu_0}{4\pi} \cdot \ln\left(\frac{D^2 - 2xD \cdot cos(\beta) + x^2}{r^2 - 2xr \cdot cos(\beta) + x^2}\right) + \frac{\mu_0}{2\pi} \cdot \left(\ln\left(\frac{D}{r}\right)\right)$$

$$L_{ba} = 1x10^{-7} + 1x10^{-7}\ln\left(\frac{D^2 - 2xD \cdot cos(\beta) + x^2}{r^2 - 2xr \cdot cos(\beta) + x^2}\right) + 2x10^{-7}\left(\ln\left(\frac{D}{r}\right)\right)$$

$$L_{ba} = 1x10^{-7} + 1x10^{-7}\ln\left(\frac{D^2 - 2xD \cdot cos(\beta) + x^2}{r^2 - 2xr \cdot cos(\beta) + x^2}\right) + 2x10^{-7}\ln\left(\frac{D}{r}\right)$$

$$L_{ba} = 1x10^{-7} + 1x10^{-7}\left(\ln\left(\frac{D^2 - 2xD \cdot cos(\beta) + x^2}{r^2 - 2xr \cdot cos(\beta) + x^2}\right) + 2\ln\left(\frac{D}{r}\right)\right)$$

$$L_{ba} = 1x10^{-7}\left(1 + \ln\left(\frac{D^2 - 2xD \cdot cos(\beta) + x^2}{r^2 - 2xr \cdot cos(\beta) + x^2}\right) + \ln\left(\frac{D}{r}\right)^2\right)$$

$$L_{ba} = 1x10^{-7}\left(1 + \ln\left(\frac{D^2(D^2 - 2xD \cdot cos(\beta) + x^2)}{r^2(r^2 - 2xr \cdot cos(\beta) + x^2)}\right)\right) \qquad (26)$$

This is the equation for the mutual inductance element L_{ba} and its mirror image L_{bc}.

Replacing the generic notations ‘x’ and ‘D’ with their specific distance:

x = distance between conductors ‘a’ and ‘b’ = ‘D_{ab}’

D = distance between conductors ‘a’ and ‘p’ (line integral distance) = ‘D_{ap}’

$$L_{ba} = 1x10^{-7}\left(1 + \ln\left(\frac{D_{ap}{}^2(D_{ap}{}^2 - 2D_{ab}D_{ap} \cdot cos(\beta) + D_{ab}{}^2)}{r^2(r^2 - 2D_{ab}r \cdot cos(\beta) + D_{ab}{}^2)}\right)\right) \qquad (27)$$

3.5.1.3 *Flux linkage from the current in circuit a-p with circuit c-p*

The next requirement is to integrate conductor 'a' and 'p' flux densities along line c-p, represented in Figure 10.

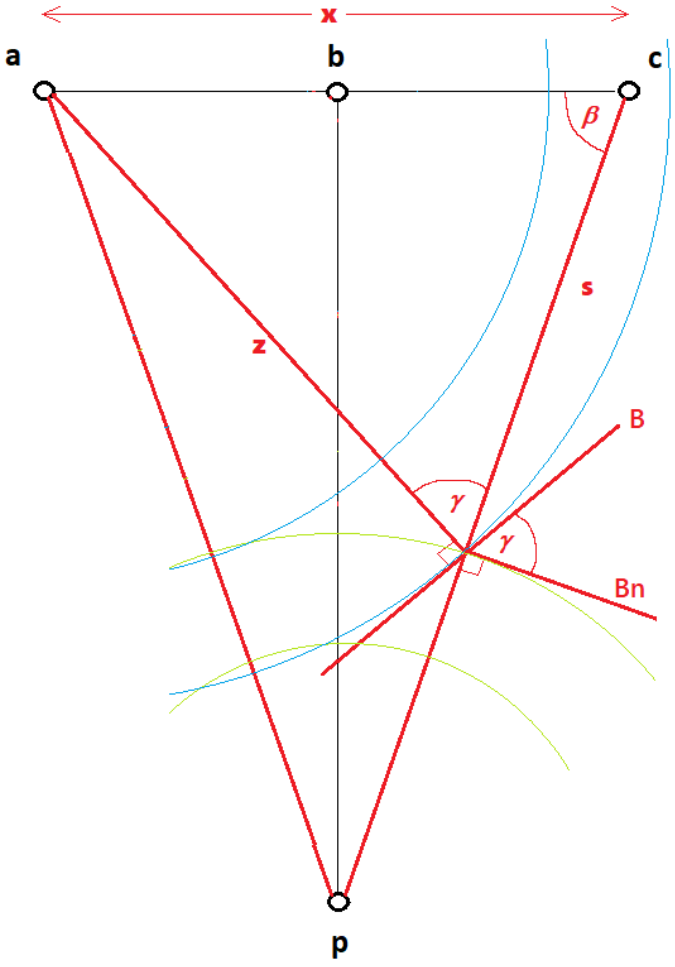

Figure 10. Geometry of the tower conductor arrangement, showing the three phases at the top, and an earth-return ('p') at the bottom. The circular lines represent flux direction from conductor 'a' (blue) and 'p' (green). The angle at which they cross the normal ('Bn') to circuit c-p is designated 'γ'.

It is evident that the same trigonometric process can be applied as for Figure 8. This leads to the exact same equation structure as L_{ba} (26) for L_{ac} (and L_{ca}):

$$L_{ac} = 1x10^{-7}\left(1 + \ln\left(\frac{D^2(D^2-2xD\cdot cos(\beta)+x^2)}{r^2(r^2-2xr\cdot cos(\beta)+x^2)}\right)\right) \qquad (28)$$

However, again the generic notations 'x' and 'D' represent different distances in (28) than in (26):

x = distance between conductors 'a' and 'c' = 'D_{ac}'

D = distance between conductors 'c' and 'p' (line integral distance) = 'D_{cp}'

$$L_{ca} = 1x10^{-7}\left(1 + \ln\left(\frac{D_{cp}{}^2(D_{cp}{}^2 - 2D_{ac}D_{cp}\cdot cos(\beta) + D_{ac}{}^2)}{r^2(r^2 - 2D_{ac}r\cdot cos(\beta) + D_{ac}{}^2)}\right)\right) \quad (29)$$

3.5.2 Symmetric Arrangement

The self-inductance equation for the symmetric system is the same one presented in the asymmetric system (5):

$$L_{self} = 4x10^{-7}\left(\ln\left(\frac{D}{r'}\right)\right)$$

where r' = equivalent radius = 0.7788r

(to simplify internal plus external inductance components)

To find the mutual flux linkages, consider the following derivation example to find the flux linkage from the current in circuit a-p with circuit b-p:

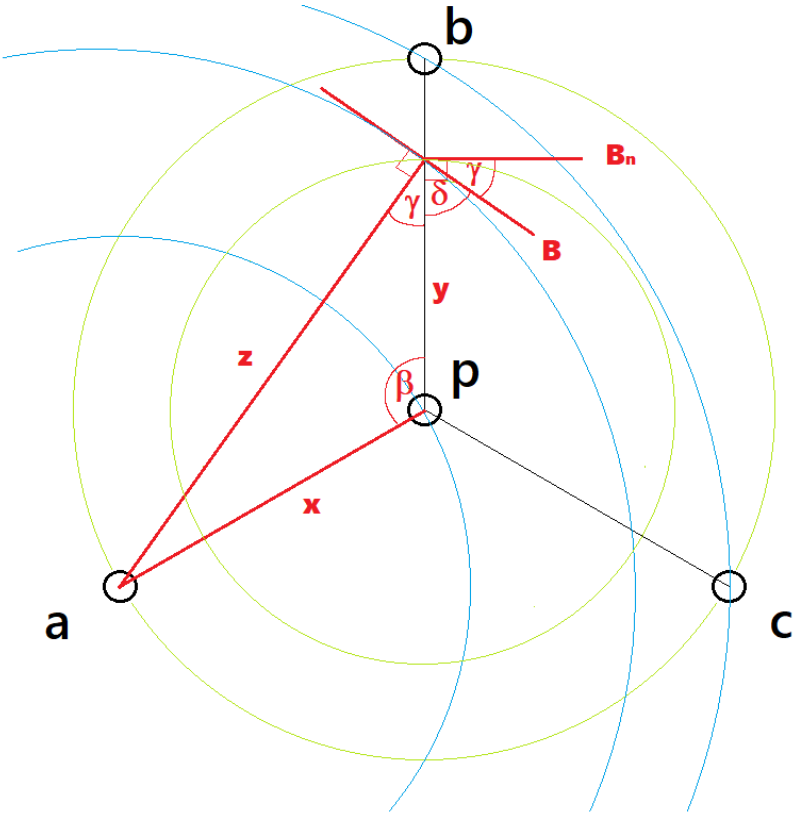

Figure 11. Geometry of the tower conductor arrangement, showing the three phases around the outside, and a central earth-return ('p'). The circular lines represent flux direction from conductor 'a' (blue) and 'p' (green). The angle at which they cross the normal ('Bn') to circuit b-p is designated 'γ'.

Circuit a-p consists of the current flowing in conductor ‘a’ and its earth-return equivalent ‘p’. The flux density of conductor ‘a’ relative to the normal of the line integral b-p is needed. Starting with the standard equation (7):

$$B = \frac{\mu_0 I_a}{2\pi z}$$

where z = distance from conductor ‘a’.

Taking the angle into account, B_n is required (not B), which is the component of I_a that is normal to b-p:

$$Bn = \frac{\mu_0 I_a \cdot cos(\gamma)}{2\pi z}$$

Repeating the exact same derivation represented from equations (15) through to (26), except replacing variable labels ‘I_b’ for ‘I_a’ and ‘s’ for ‘y’, it ends up with the same equation as (26):

$$L_{mutual} = 1x10^{-7}\left(1 + \ln\left(\frac{D^2(D^2 - 2xD \cdot cos(\beta) + x^2)}{r^2(r^2 - 2xr \cdot cos(\beta) + x^2)}\right)\right)$$

However, again, the distances that ‘D and ‘x’ represent are different than previous. In the symmetric system, subscripts aren’t needed to denote specific distances because all phase distances to each other and to their earth-returns are equal, so keeping the generic notations:

x = distance between phase conductors; and

D = distance between phase and earth-return conductors.

This mutual inductance equation of the ideal symmetric system represents all mutual inductance elements.

Next, the distances ‘D’ and ‘x’ were defined for the symmetric system. To make it as similar as possible to the asymmetric system, the geometric mean distances from the asymmetric system were used:

Asymmetric GMD = $\sqrt[3]{(D_{ab}D_{ac}D_{bc})}$

This GMD was used as distance 'x' between symmetric system phase conductors. Using simple trigonometry, the distance 'D' between any phase conductor and the central earth-return conductor is:

$$D = \frac{x/2}{\cos(30°)}$$

3.6 Capacitance Matrix of the Transmission Line

The 3x3 capacitance matrix was required next. Just like the inductance matrix, the main diagonal and off-diagonal elements represent the self and mutual capacitances, respectively.

The self-capacitances can be calculated directly with standard equations for a two-wire circuit:

The potential difference (voltage) is the work (W) done on a charge (q) to move it in an electric field from one point of potential to a different point of potential. It is dependent on the electric field intensity (E), which is the force (N) per unit charge (Coulomb).

The potential difference (voltage) between two points is defined as the work done (W) on a charge (q) of 1 Coulomb to move it from one point to the other.

It is dependent on the electric field intensity: $E = \frac{q}{2\pi x\varepsilon}$ V/m

To find the voltage between the two points, E must be integrated along the line between the two points:

$V_{12} = \int_{D_1}^{D_2} E\ dx$ where D = radial distance between point and conductor centre.

$$V_{12} = \int_{D_1}^{D_2} \frac{q}{2\pi x\varepsilon}\ dx$$

$$V_{12} = \frac{q}{2\pi\varepsilon}\int_{D_1}^{D_2} \frac{1}{x}\ dx$$

$$V_{12} = \frac{q}{2\pi\varepsilon}\left[\ln\left(\frac{D_2}{D_1}\right)\right]$$

Applying the above to a two-wire circuit and using superposition to add the two components:

(i) Pushing the charge on conductor 1 (q_1) from conductor 1 to conductor 2:

Potential difference due to charge on conductor 1 only = $\frac{q_1}{2\pi\varepsilon}\left[\ln\left(\frac{D}{r_1}\right)\right]$

(ii) Pushing the charge on conductor 2 (q_2) *also* from conductor 1 to conductor 2:

Potential difference due to charge on conductor 2 (q_2) only = $\frac{q_2}{2\pi\varepsilon}\left[\ln\left(\frac{r_2}{D}\right)\right]$

where D = distance between conductors; and

r = radius of conductor

ε = permittivity of free space = 8.854 x 10^{-12} F/m

Superposition of the above two potential difference components gives the voltage with respect to ground of the 2-wire system:

$$V_{12} = \frac{q_1}{2\pi\varepsilon}\ln\left(\frac{D}{r_1}\right) + \frac{q_2}{2\pi\varepsilon}\ln\left(\frac{r_2}{D}\right)$$

$$V_{12} = \frac{1}{2\pi\varepsilon}\left[q_1\ln\left(\frac{D}{r_1}\right) + q_2\ln\left(\frac{r_2}{D}\right)\right]$$

Since the 2-wire earth-return model has (i) identical phase and earth-return conductors, and the current around the loop is constant (ii), then:

(i) $r_1 = r_2 =$ 'r'

(ii) $q_2 = -q_1$

Applying (i) and (ii) above, the standard voltage per unit length equation becomes:

$$V_{12} = \frac{1}{2\pi\varepsilon}\left[q_1\ln\left(\frac{D}{r}\right) - q_1\ln\left(\frac{r}{D}\right)\right]$$

$$V_{12} = \frac{1}{2\pi\varepsilon}\left[q_1\ln\left(\frac{D}{r}\right) + q_1\ln\left(\frac{D}{r}\right)\right]$$

$$V_{12} = \frac{1}{2\pi\varepsilon}\cdot 2\left[q_1\ln\left(\frac{D}{r}\right)\right]$$

$$V_{12} = \frac{q_1}{\pi\varepsilon}\left[\ln\left(\frac{D}{r}\right)\right] \qquad (30)$$

Capacitance per unit length:

$$C_{12} = \frac{q_1}{V_{12}} = \frac{\pi\varepsilon}{\ln\left(\frac{D}{r}\right)} \qquad (31)$$

For the mutual capacitance elements, the first step was to calculate the voltage on one circuit caused by charges on another circuit. Next was to convert voltage matrices to capacitance matrices.

The simple relationship $C = \frac{q}{V}$ needs to be applied with care when dealing with matrices, because division can't be applied directly.

Starting with q = CV:

$$\begin{bmatrix} C_{ap} & C_{ab} & C_{ac} \\ C_{ba} & C_{bp} & C_{bc} \\ C_{ca} & C_{cb} & C_{cp} \end{bmatrix} \cdot \begin{bmatrix} V_{ap} \\ V_{bp} \\ V_{cp} \end{bmatrix} = \begin{bmatrix} q_a \\ q_b \\ q_c \end{bmatrix}$$

The divide operator can't be applied to rearrange matrices, so an inverse matrix is used to rearrange the equation. In other words, instead of having $V = \frac{q}{C}$, it must be V = Pq, where $P = C^{-1}$:

$$\begin{bmatrix} P_{ap} & P_{ab} & P_{ac} \\ P_{ba} & P_{bp} & P_{bc} \\ P_{ca} & P_{cb} & P_{cp} \end{bmatrix} \cdot \begin{bmatrix} q_a \\ q_b \\ q_c \end{bmatrix} = \begin{bmatrix} V_{ap} \\ V_{bp} \\ V_{cp} \end{bmatrix}$$

To find P_{ap} above, make q_a = 1 Coulomb while the other charges are zero. This gives the equation:

$$P_{ap} q_a = V_{ap}$$

Substituting in the value for q_a: $P_{ap} = V_{ap}$

To find P_{ab}, make q_b = 1 C and the other charges zero, yielding the equation: $P_{ab} = V_{bp}$ etc.

To finally convert the P matrix to the C matrix, it is simply inverted. Note that this is *not* the same as inverting the elements individually.

3.6.1 Asymmetric Arrangement

3.6.1.1 Potential difference on circuit b-p caused by charges from circuit a-p.

To evaluate the potential difference across circuit b-p caused by charges on circuit a-p *only*, the charge on the phase 'a' conductor was made equal to 1 Coulomb, while all other phases have zero charge:

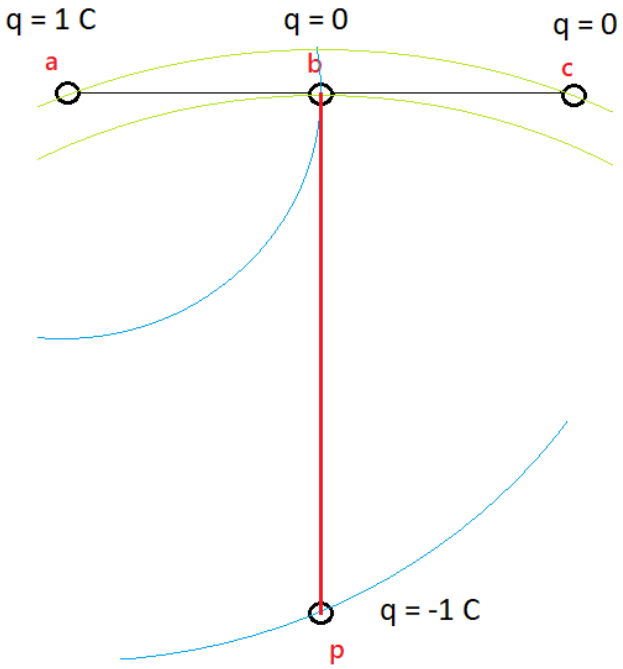

Figure 12. Geometry of the tower conductor arrangement, showing the three phases at the top, and an earth-return ('p') at the bottom. The curved lines represent equipotentials in the electric fields created by charges on conductor 'a' (blue) and 'p' (green). The resulting potential differences across circuit b-p (red line) are derived.

Integrating the electric field differences along line b-p:

$$V_{ba} = \frac{q_a}{2\pi\varepsilon}\ln\left(\frac{D_{ap}}{D_{ab}}\right) + \frac{q_p}{2\pi\varepsilon}\ln\left(\frac{r}{D_{bp}}\right)$$

Substitute in charge values (Figure 12):

$$V_{ba} = \frac{1}{2\pi\varepsilon}\ln\left(\frac{D_{ap}}{D_{ab}}\right) + \frac{-1}{2\pi\varepsilon}\ln\left(\frac{r}{D_{bp}}\right)$$

$$V_{ba} = \frac{1}{2\pi\varepsilon}\ln\left(\frac{D_{ap}}{D_{ab}}\right) + \frac{1}{2\pi\varepsilon}\ln\left(\frac{D_{bp}}{r}\right)$$

$$V_{ba} = \frac{1}{2\pi\varepsilon}\ln\left(\frac{D_{ap}D_{bp}}{D_{ab}r}\right) \qquad (32)$$

3.6.1.2 Potential difference on circuit a-p caused by charges from circuit b-p.

The previous arrangement was flipped, making the charge on the phase 'b' conductor equal to 1 Coulomb while all other phases have zero charge:

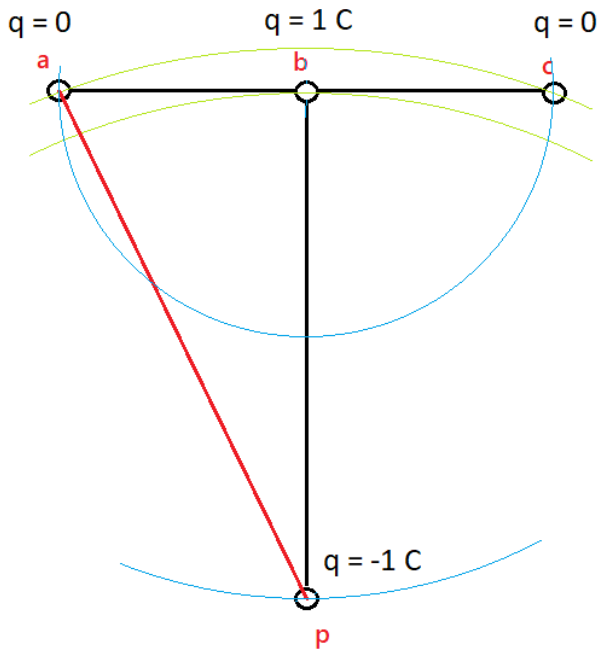

Figure 13. Geometry of the tower conductor arrangement, showing the three phases at the top, and an earth-return ('p') at the bottom. The curved lines represent equipotentials in the electric fields created by charges on conductor 'b' (blue) and 'p' (green). The resulting potential differences across circuit a-p (red line) are derived.

Integrating the electric field differences along line a-p:

$$V_{ab} = \frac{q_b}{2\pi\varepsilon}\ln\left(\frac{D_{bp}}{D_{ab}}\right) + \frac{q_p}{2\pi\varepsilon}\ln\left(\frac{r}{D_{ap}}\right)$$

Substitute in charge values (Figure 13):

$$V_{ab} = \frac{1}{2\pi\varepsilon}\ln\left(\frac{D_{bp}}{D_{ab}}\right) + \frac{-1}{2\pi\varepsilon}\ln\left(\frac{r}{D_{ap}}\right)$$

$$V_{ab} = \frac{1}{2\pi\varepsilon}\ln\left(\frac{D_{bp}}{D_{ab}}\right) + \frac{1}{2\pi\varepsilon}\ln\left(\frac{D_{ap}}{r}\right)$$

$$V_{ab} = \frac{1}{2\pi\varepsilon}\ln\left(\frac{D_{bp}D_{ap}}{D_{ab}r}\right) \qquad (33)$$

Note that V_{ab} (33) and V_{ba} (32) are identical. Due to the symmetric geometry of phases 'a' and 'c' about phase 'b', the above equation also applies for V_{cb} and V_{bc}.

3.6.1.3 *Potential difference on circuit a-p caused by charges from circuit c-p.*

Finally, making the charge on the phase 'c' conductor equal to 1 Coulomb while all other phases have zero charge:

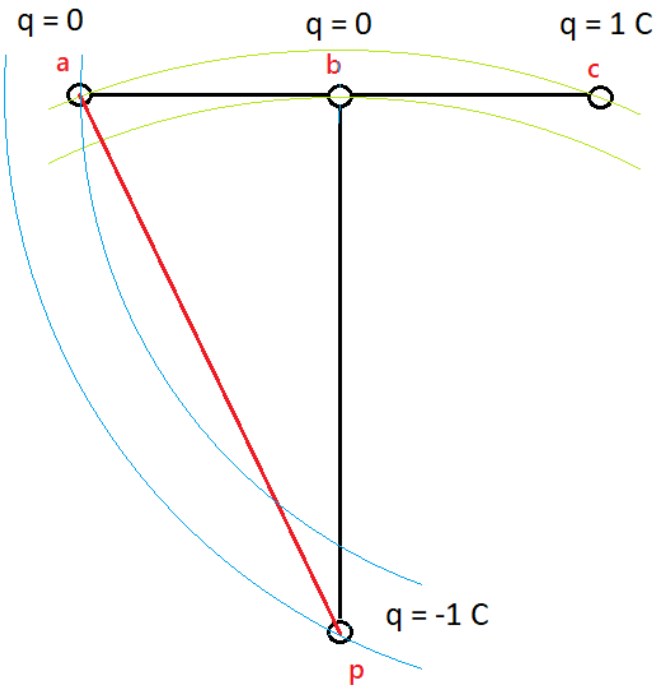

Figure 14. Geometry of the tower conductor arrangement, showing the three phases at the top, and an earth-return ('p') at the bottom. The curved lines represent equipotentials in the electric fields created by charges on conductor 'c' (blue) and 'p' (green). The resulting potential differences across circuit a-p (red line) are derived.

Integrating the electric field differences along line a-p:

$$V_{ac} = \frac{q_c}{2\pi\varepsilon}\ln\left(\frac{D_{cp}}{D_{ac}}\right) + \frac{q_p}{2\pi\varepsilon}\ln\left(\frac{r}{D_{ap}}\right)$$

Substitute in charge values (Figure 13):

$$V_{ac} = \frac{1}{2\pi\varepsilon}\ln\left(\frac{D_{cp}}{D_{ac}}\right) + \frac{-1}{2\pi\varepsilon}\ln\left(\frac{r}{D_{ap}}\right)$$

$$V_{ac} = \frac{1}{2\pi\varepsilon}\ln\left(\frac{D_{cp}}{D_{ac}}\right) + \frac{1}{2\pi\varepsilon}\ln\left(\frac{D_{ap}}{r}\right)$$

$$V_{ac} = \frac{1}{2\pi\varepsilon}\ln\left(\frac{D_{cp}D_{ap}}{D_{ac}r}\right)$$

Note that $D_{cp} = D_{ap}$, so:

$$V_{ac} = \frac{1}{2\pi\varepsilon}\ln\left(\frac{D_{ap}^2}{D_{ac}r}\right) \quad (34)$$

3.6.2 Symmetric Arrangement

In the balanced symmetric arrangement, all mutual capacitances will be equal. It doesn't matter which mutual inductance is derived, and the following was randomly chosen.

3.6.2.1 Potential difference on circuit b-p caused by charges from circuit a-p.

Making the charge on the phase 'a' conductor equal to 1 Coulomb while all other phases have zero charge:

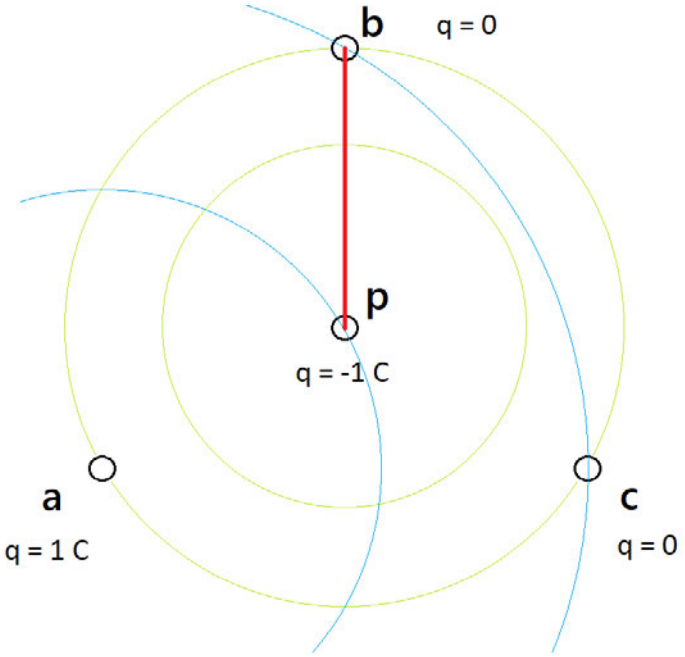

Figure 15. Geometry of the tower conductor arrangement, showing the three phases around the outside, and a central earth-return ('p'). The curved lines represent equipotentials in the electric fields created by charges on conductor 'a' (blue) and 'p' (green). The resulting potential differences across circuit b-p (red line) are derived.

Integrating the electric field differences along line b-p:

$$V_{ba} = \frac{q_a}{2\pi\varepsilon}\ln\left(\frac{D_{ap}}{D_{ab}}\right) + \frac{q_p}{2\pi\varepsilon}\ln\left(\frac{r}{D_{bp}}\right)$$

Substitute in charge values (Figure 15):

$$V_{ba} = \frac{1}{2\pi\varepsilon}\ln\left(\frac{D_{ap}}{D_{ab}}\right) + \frac{-1}{2\pi\varepsilon}\ln\left(\frac{r}{D_{bp}}\right)$$

$$V_{ba} = \frac{1}{2\pi\varepsilon}\ln\left(\frac{D_{ap}}{D_{ab}}\right) + \frac{1}{2\pi\varepsilon}\ln\left(\frac{D_{bp}}{r}\right)$$

$$V_{ba} = \frac{1}{2\pi\varepsilon}\ln\left(\frac{D_{ap}D_{bp}}{D_{ab}r}\right)$$

Note that $D_{ap} = D_{bp}$, so:

$$V_{ba} = \frac{1}{2\pi\varepsilon}\ln\left(\frac{D_{ap}^2}{D_{ab}r}\right) \quad (35)$$

CHAPTER 4

RESULTS AND DISCUSSION

Both analytical and simulation explorations were to be conducted side by side to correlate and verify each other. Firstly, the 'proof of concept' verifications of simple simulation circuits with classical theory needed establishing. Then the derived models could be simulated to explore the effects of asymmetry on travelling wave velocity.

Any evidence that emerged of different travelling wave propagation speeds between models needed careful analysis in relation to measurement and inherent model error, as well as comparability between models that are fundamentally different in ways outside of symmetry.

4.1 Initial Single Phase Test Circuit

The following was the initial single-phase testing of the simulation with basic mathematical correlation checks. This was DC for ease of initial testing clarity, and didn't yet include a fault in the centre of the line. It was just sending a pulse down the line and back to observe propagation.

Figure 16 (over page) represents the voltage of the line measured over time. Using V4 as an example (top trace, representing the measurement taken one section down from the line start seen on Figure 4, page 20), it can be seen that the initial step of 100 V hit the sensor at time = 1.03×10^{-3} seconds (highlighted measurement #1 on right). It doubled at time = 7.196×10^{-3} seconds (measurement #2), due to the reflection coming back from the end of the entire line and adding to the incident step. The reflection was equal in magnitude because the open circuit termination represents a reflection coefficient of 1.

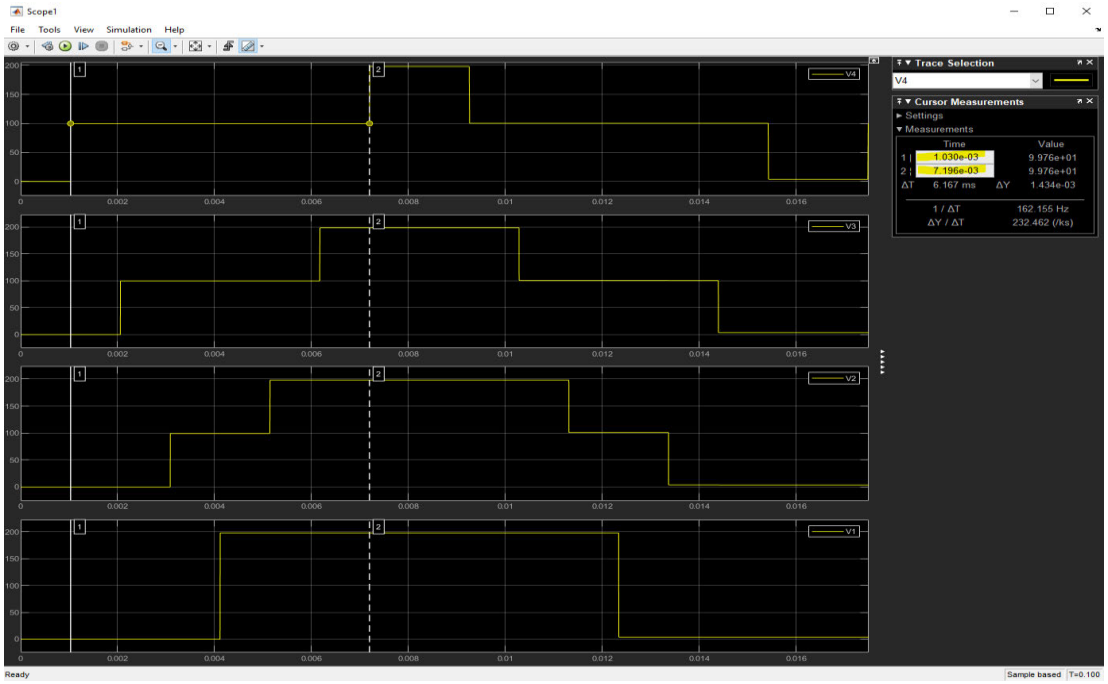

Figure 16. Initial testing of the Simulink model shown in Figure 4, with voltage measurements over time taken at different sections of the line (V1-V4).

Checking the time measurements above with the theoretical propagation velocity (v_p):

$$v_p = \frac{1}{\sqrt{LC}}$$ where L = inductance per unit length (H/m); and

C = capacitance per unit length (F/m)

**NOTE: this is for high frequency approximation. It comes from assumed lossless propagation constant applicable at high frequencies (de Magalhães Júnior & Lopes 2021):*

$$\gamma = \cancel{\alpha} + j\beta = \sqrt{(\cancel{R} + j\omega L)(\cancel{G} + j\omega C)}$$

where α = attenuation coefficient, associated with R and G, lossless/disregarded at high frequencies, simplifying the equation to:

$$\gamma = \beta = \sqrt{(\omega L)(\omega C)}$$

$$\gamma = \beta = \omega\sqrt{LC}$$

and $v_p = \frac{\omega}{\beta}$ (1)

therefore, $v_p = \frac{1}{\sqrt{LC}}$

The values for inductance (L) and capacitance (C) per unit length (km) were left as default (below):

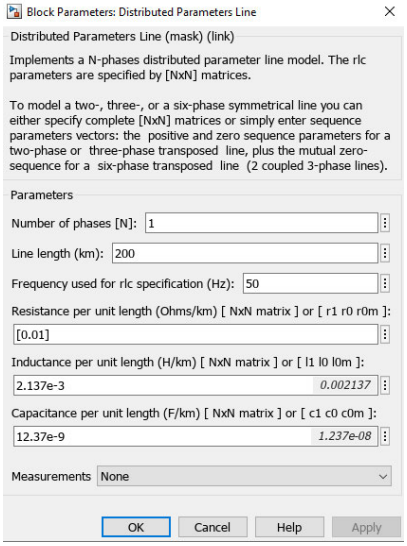

Figure 17. The block input fields for the distributed parameter line sections. Values left as default for initial testing. Note the L and C parameters are per km.

Therefore:

$$v_p = \frac{1}{\sqrt{2.137x10^{-3} - 3\ x\ 12.37x10^{-9}}}$$

v_p = 194 497 km/s

$$\text{Time taken (t)} = \frac{distance}{v_p}$$

The distance that the signal must travel from the sending end to reach the sensor was 200 km, so the time taken:

$$t = \frac{200}{194497}$$

t = 0.00103 s → matches measurement #1 (Figure 16)

The distance that the reflected signal must travel up and back again from the sending end to reach the sensor is 1400 km, so the time taken:

$$T = \frac{1400}{194497}$$

T = 0.00720 s → matches measurement #2 (Figure 16)

This initial test correlated the simulation results with theory. Next was to calculate and apply appropriate L and C values and resultant propagation velocity.

4.2 Classical Single Phase

Starting simple, the propagation velocity in a single-phase system was investigated using classical equations. The 'speed of light' (***c***) is the upper limit of propagation velocity:

$$\boldsymbol{c} = 2.998 \times 10^8 \text{ m/s.}$$

Propagation velocity standard equation:

$$v_p = \frac{1}{\sqrt{LC}} \qquad \text{m/s}$$

The propagation velocity is therefore inversely proportional to the product of inductance and capacitance.

Inductance standard equation for 2-wire line (5):

$$L = 4x10^{-7}\left(\ln\left(\frac{D}{r'}\right)\right) \qquad \text{H/m}$$

Where r' = conductor equivalent radius = 0.7788r

Capacitance standard equation for 2-wire line (31):

$$\mathrm{C} = \frac{\pi\varepsilon}{\ln\left(\frac{D}{r}\right)} \qquad \text{F/m}$$

4.2.1 Choice of value for conductor distance *D*

To make the single-phase testing as similar as the asymmetric 3-phase model following later, the conductor distance ***D*** was chosen as the average earth-return conductor distance ***D*** of the latter model, which is based on the 25 kV tower geometry example in the Simulink in-built 'Line Parameter Calculator' application.

D = 10.4189 m, which gives:

L = 2.880×10^{-06} H/m

C = 4.003×10^{-12} F/m

$v_p = 2.945 \times 10^8$ m/s.

A similar velocity result was obtained on the simulator (Figure 18 below) with the above L and C parameters:

**Note, testing changed to AC in lieu of the 3-phase model to follow. The concept remains the same, with the voltage steps occurring on top of the native 50 Hz signal.*

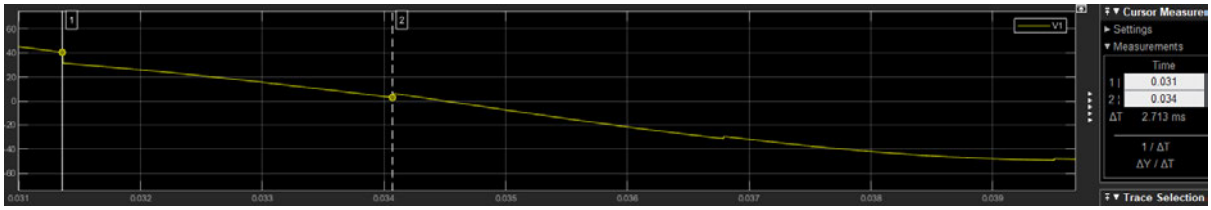

*Figure 18. Simulated single-phase transmission line with fault, over a zoomed-in section of the 50 Hz sine wave. The L and C values previous were entered into the distributed parameters line sections. The trace measurement lines (vertical full and dashed) show travelling wave peaks for conductor distance **D** used in the asymmetric system. The time interval between peaks (ΔT displayed on right) averaged 2.715 ms, which equates to 2.947 x 10^8 m/s.*

The propagation velocity with respect to light speed in the above single-phase example is 0.98***c***. This seemed reasonable, so testing progressed to the 3-phase model.

4.3 Three-Phase System

The 3x3 inductance and capacitance matrices were constructed using the derived formulas from the Methodology section (equations 5, 14, 26, 27, 29, 31, 32, 33, 34, 35). These were entered into the input fields of the distributed parameter line section blocks of the 3-phase Simulink model (Figure 5, page 21).

4.3.1 Initial 3-Phase Results

The following is a simulator comparison of travelling wave propagation velocity in the derived symmetric and asymmetric models. Table 1 represents travelling wave peak intervals (which are inversely proportional to velocity) for different fault types tested on both symmetric and asymmetric models. These initial results suggested that the symmetric system had a faster propagation velocity than the asymmetric (shorter peak intervals), on average by 1.1%. A single percentage is a small proportion, but it must be kept in context with the near light speeds and resulting distances involved. For example, the 1.1% difference in velocities results in a fault-locating difference of nearly 9 km.

*Table 1. Average phase peak intervals for the first four groups of waves, measured for different fault types on both symmetric and asymmetric models. The latter is **not** the zeroth-order (averaged) model introduced in Section 3.2.*

	Fault type	Interval between peaks (ms)	
		Symmetric	Asymmetric
Ground Faults	L-G	2.639	2.669
	L-L-G	2.649	2.675
	L-L-L-G	2.637	2.667
Non-Ground Faults	L-L	2.649	2.678
	L-L-L	2.636	2.667
	Single Open	2.639	2.668
	Double Open	2.638	2.668
	Triple Open	2.638	2.668

There was some variation within each model (except for the open circuit faults) that may have initially suggested different propagation velocities per fault type, however, there was peak ambiguity involved. For example, first consider the measurement of well-defined peaks that emerged for the open circuit faults:

Symmetric:

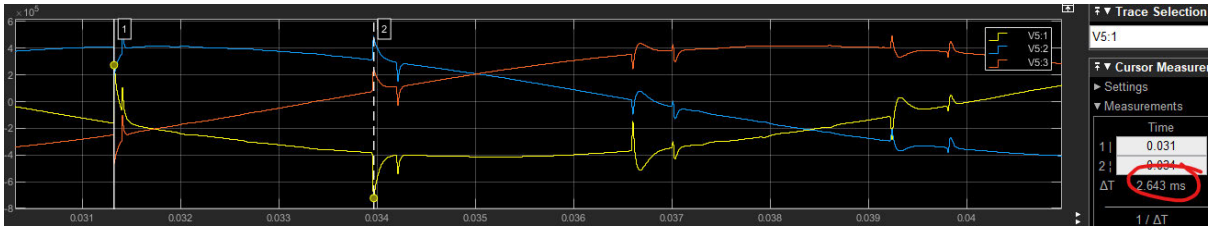

Figure 19. Travelling waveforms for the single-phase open circuit fault on the symmetric model. Time interval between first and second wave groups (ΔT) displayed on right (2.643 ms).

Asymmetric:

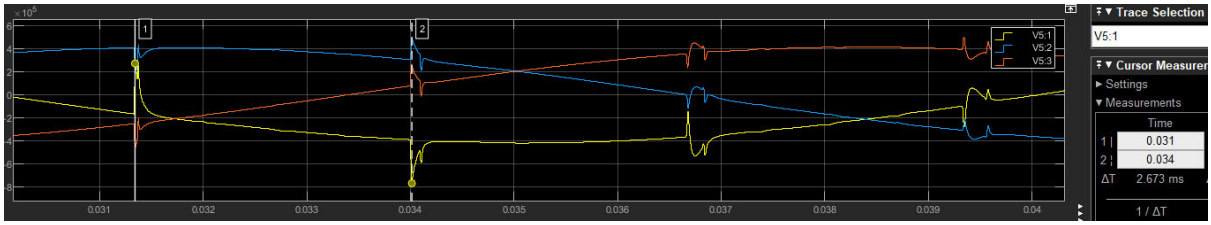

Figure 20. Travelling waveforms for the single-phase open circuit fault on the asymmetric model. Time interval between waves (ΔT) displayed on right (2.673 ms).

The distinct peaks gave measurement confidence. In contrast, the following shows some typical peak ambiguity issues that were common in non-open circuit fault peak measurements, and cast doubt on the initial variation displayed in Table 1:

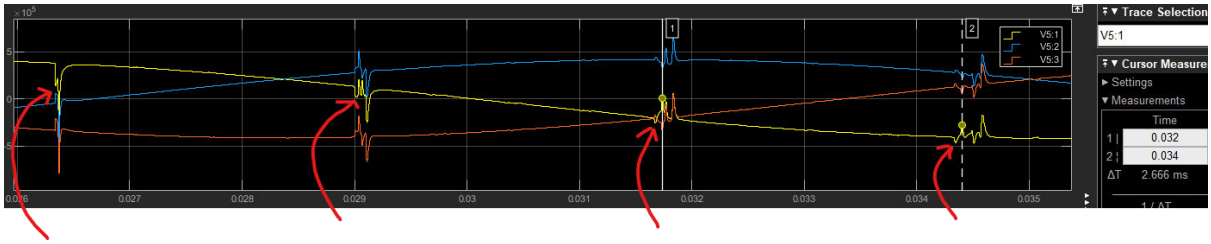

Figure 21. Travelling waveforms for the L-G fault on the asymmetric model highlighting the peak ambiguity problem (red arrows). The symmetric model displayed very similar. The first arrow shows a relatively very minor peak just before the main. The second arrow shows rounded non-distinct first peak compared to the second. The 3rd and 4th arrows show again very minor initial peaks compared to the second.

Therefore, there was still confidence that the symmetric system produced a faster travelling wave than the asymmetric, especially due to the open fault peak clarity, however there was no confidence in the initial suggestion of a different travelling wave velocity for different fault types.

In an attempt to address the peak ambiguity problem and investigate if any variation was more than just measurement error, the lines were made lossless and the Clarke transformation was applied (this is the αβ0 function block in Figure 5, page 21).

4.3.2 Lossless Lines

The following is a typical example of attempting to address the previously ambiguous peaks. Again comparing the symmetric and asymmetric, but now also including the Clarke transformation.

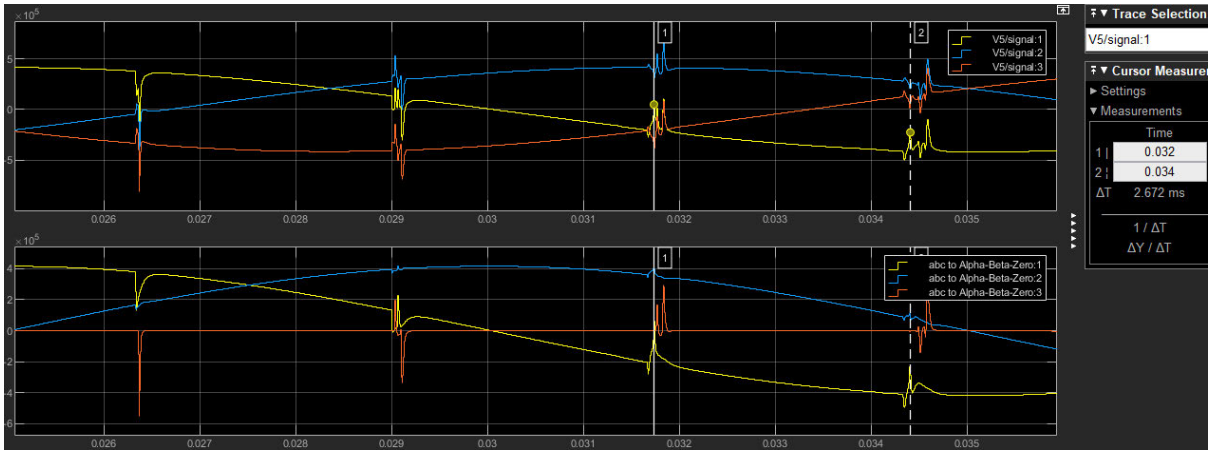

Figure 22. Travelling waveforms for the L-G fault on the asymmetric lossless model. The top trace is the 3 phases a, b and c, and the bottom trace is the 3 modes α, β and 0. Compared to the previous Figure 21, the lossless lines didn't improve the phase trace peak issues. The modes on the bottom also retained those issues, except for the first peak.

Comparing the lossless and transformed version above (Figure 22) to the previous Figure 21, the lossless lines didn't improve the phase (top trace) peak issues. The modes (bottom trace) also retained those issues, except for the first peak. These issues remained in both asymmetric and symmetric models.

The Clarke transformation trace didn't help. Therefore, the peak ambiguity problem persisted, and any of the initial variation between fault type velocities displayed in Table 1 remains likely measurement error.

Next was the analytical approach. This employed the 'zeroth order' averaging method described on page 19 to decouple asymmetric system.

4.4 Analytical Investigation

This was still an attempt to verify simulation results and address the ambiguous peak measurement issue from the simulations. This again used the 3x3 L and C matrices constructed from the derived 3-phase models. The process below is described in the Methodology section on pages 18 and 19.

4.4.1 Asymmetric System

Starting with the derived L and C matrices:

$$[L] = \begin{bmatrix} L_a & L_{ab} & L_{ac} \\ L_{ba} & L_b & L_{bc} \\ L_{ca} & L_{cb} & L_c \end{bmatrix} \qquad [C] = \begin{bmatrix} C_a & C_{ab} & C_{ac} \\ C_{ba} & C_b & C_{bc} \\ C_{ca} & C_{cb} & C_c \end{bmatrix}$$

Using the derived formulas (Methodology section) to fill in the above elements:

$$L = \begin{bmatrix} 0.2880 & 0.1916 & 0.1779 \\ 0.1916 & 0.2878 & 0.1916 \\ 0.1779 & 0.1916 & 0.2880 \end{bmatrix} \text{x}10^{-5}\ \text{H/m} \qquad C = \begin{bmatrix} 0.7717 & -0.3489 & -0.2381 \\ -0.3489 & 0.8567 & -0.3489 \\ -0.2381 & -0.3489 & 0.7717 \end{bmatrix} \text{x } 10^{-11}\ \text{F/m}$$

The impedance and admittance matrices were obtained as follows:

$[Z] = j\omega L$ $\qquad$ $[Y] = j\omega C$

$$[Z] = \begin{bmatrix} 0.0000 + 0.9049i & 0.0000 + 0.6019i & 0.0000 + 0.5588i \\ 0.0000 + 0.6019i & 0.0000 + 0.9040i & 0.0000 + 0.6019i \\ 0.0000 + 0.5588i & 0.0000 + 0.6019i & 0.0000 + 0.9049i \end{bmatrix} \text{x}10^{-3} \text{ Ohms/m}$$

$$[Y] = \begin{bmatrix} 0.0000 + 0.2424i & 0.0000 - 0.1096i & 0.0000 - 0.0748i \\ 0.0000 - 0.1096i & 0.0000 + 0.2691i & 0.0000 - 0.1096i \\ 0.0000 - 0.0748i & 0.0000 - 0.1096i & 0.0000 + 0.2424i \end{bmatrix} \text{x}10^{-8} \text{ Mhos/m}$$

$$[Z][Y] = \begin{bmatrix} -0.1116 & -0.0016 & -0.0018 \\ -0.0018 & -0.1114 & -0.0018 \\ -0.0018 & -0.0016 & -0.1116 \end{bmatrix} \text{x}10^{-11} \qquad \text{of the form} = \begin{bmatrix} x & y & z \\ w & u & w \\ z & y & x \end{bmatrix}$$

*(Note: the [Z][Y] matrix was a Matlab output, where **z** and **w** appear equal by rounding only. The more precise numbers are -1.8312x10^{-14} and -1.8336 x10^{-14}, respectively)*

Clarke transform to decouple the system:

$$\text{Clarke transformation matrix } [T] = \sqrt{\frac{2}{3}} \begin{bmatrix} 1 & -\frac{1}{2} & -\frac{1}{2} \\ 0 & \frac{\sqrt{3}}{2} & -\frac{\sqrt{3}}{2} \\ \frac{1}{\sqrt{2}} & \frac{1}{\sqrt{2}} & \frac{1}{\sqrt{2}} \end{bmatrix}$$

Decoupling Transformation:

$$[T][Z][Y][T]^{-1} = \begin{bmatrix} -0.1098 & -0.0000 & 0.0000 \\ -0.0000 & -0.1098 & -0.0000 \\ -0.0002 & 0.0003 & -0.1150 \end{bmatrix} \text{x}10^{-11}$$

The system was still coupled with non-zero off-diagonal elements. Therefore, to properly decouple the system, the zeroth-order averaging method was used:

$$\text{This method changes the unbalanced form } [ZY] = \begin{bmatrix} x & y & z \\ w & u & w \\ z & y & x \end{bmatrix}$$

$$\text{to the balanced form } [ZY]_{bal} = \begin{bmatrix} h & m & m \\ m & h & m \\ m & m & h \end{bmatrix}$$

Where the main diagonal elements $h = \frac{x+u+x}{3}$; and the off-diagonal elements $m = \frac{w+y+z}{3}$
Now,

$$[ZY]_{bal} = \begin{bmatrix} -0.1115 & -0.0017 & -0.0017 \\ -0.0017 & -0.1115 & -0.0017 \\ -0.0017 & -0.0017 & -0.1115 \end{bmatrix} \text{x}10^{-11}$$

Naturally, this represented an accuracy compromise, but is necessary to properly decouple the system with the Clarke transform:

$$[T][ZY]_{bal}[T]^{-1} = \begin{bmatrix} -0.1098 & 0 & 0 \\ 0 & -0.1098 & 0 \\ 0 & 0 & -0.1150 \end{bmatrix} \text{x}10^{-11}$$

Note that all the off-diagonal elements are zero. The matrix is now of the form $= \begin{bmatrix} \lambda_\alpha & 0 & 0 \\ 0 & \lambda_\beta & 0 \\ 0 & 0 & \lambda_0 \end{bmatrix}$,

Where the main diagonal represents the squared propagation constants of each mode, i.e.:

$\lambda_\alpha = \gamma_\alpha^2 = (\alpha + j\beta)^2$ for mode α, etc.

It is a lossless line, so $\alpha = 0$; and

$\gamma = j\beta = \sqrt{\lambda}$

To find propagation velocity, use Equation 1: $v_p = \frac{\omega}{\beta}$

The propagation velocity in the asymmetric 50 Hz system:

$$v_{p\_\alpha} = \frac{2\ x\ \pi\ x\ 50}{\sqrt{\lambda}}$$

$$v_{p\_\alpha} = 299\ 806\ 142\ m/s$$

$$v_{p\_\alpha} = 299\ 806\ \text{km/s}$$

This was the value yielded by the 'zeroth order' averaging method. Here is seen a flaw in the derived model – the propagation velocity is fractionally greater than the speed of light ($\boldsymbol{c}$ = 2.9979 x10^8 m/s). This will be discussed later.

Note that the averaged asymmetrical decoupled system could not be tested on the simulator, because the L and C matrices necessary are not extractable from the balanced ZY matrix.

Comparing the calculated propagation velocity with the time intervals measured previously on the simulator:

Time interval calculation: $v_p = d/t$ where d = 800 km

$t = d/v_p$

$t = 800\,000 / 299\,806\,142$

$t = 2.668$ ms

This matched the initial findings from Table 1 (particularly the open circuit fault which displayed the distinct peaks and therefore confident measurement) to at least 3 decimal places. This similarity between balanced calculated and non-balanced simulated speed suggested that there was a very low accuracy compromise when using the averaging method to allow decoupling of the modes to calculate propagation velocity.

With this verification, the next step was to compare the calculated averaged asymmetric model velocity with that of the symmetric model. Therefore, the above process was repeated for the symmetric system (below), and results compared.

4.4.2 Symmetric System

The derived L and C matrices for the symmetric system are:

$$L = \begin{bmatrix} 0.1899 & 0.0913 & 0.0913 \\ 0.0913 & 0.1899 & 0.0913 \\ 0.0913 & 0.0913 & 0.1899 \end{bmatrix} \text{x}10^{-5} \text{ H/m} \qquad C = \begin{bmatrix} 0.8446 & -0.2576 & -0.2576 \\ -0.2576 & 0.8446 & -0.2576 \\ -0.2576 & -0.2576 & 0.8446 \end{bmatrix} \text{ x } 10^{-11} \text{ F/m}$$

(Note, they are already balanced)

Impedance and admittance matrices:

$[Z] = j\omega L$ $[Y] = j\omega C$

$$[Z] = \begin{bmatrix} 0.0000 + 0.5966i & 0.0000 + 0.2869i & 0.0000 + 0.2869i \\ 0.0000 + 0.2869i & 0.0000 + 0.5966i & 0.0000 + 0.2869i \\ 0.0000 + 0.2869i & 0.0000 + 0.2869i & 0.0000 + 0.5966i \end{bmatrix} \text{x}10^{-3} \text{ Ohms/m}$$

$$[Y] = \begin{bmatrix} 0.0000 + 0.2653i & 0.0000 - 0.0809i & 0.0000 - 0.0809i \\ 0.0000 - 0.0809i & 0.0000 + 0.2653i & 0.0000 - 0.0809i \\ 0.0000 - 0.0809i & 0.0000 - 0.0809i & 0.0000 + 0.2653i \end{bmatrix} \text{x}10^{-8} \text{ Mhos/m}$$

$$[Z][Y] = \begin{bmatrix} -0.1119 & -0.0046 & -0.0046 \\ -0.0046 & -0.1119 & -0.0046 \\ -0.0046 & -0.0046 & -0.1119 \end{bmatrix} \text{x}10^{-11}$$

Decouple the system with the Clarke transform:

$$[T][Z][Y][T]^{-1} = \begin{bmatrix} -0.1073 & 0 & 0 \\ 0 & -0.1073 & 0 \\ 0 & 0 & -0.1211 \end{bmatrix} \text{x}10^{-11} = \begin{bmatrix} \lambda_\alpha & 0 & 0 \\ 0 & \lambda_\beta & 0 \\ 0 & 0 & \lambda_0 \end{bmatrix}$$

Velocity calculation: $\lambda_\alpha = \gamma_\alpha^2 = (\alpha + j\beta)^2$

It is a lossless line, so $\alpha = 0$ and $\gamma = j\beta = \sqrt{\lambda}$

$$v_p = \frac{\omega}{\beta}$$

The propagation velocity in the symmetric 50 Hz system:

$$v_p = \frac{2\ x\ \pi\ x\ 50}{\sqrt{\lambda}}$$

$$v_{p\_\alpha} = 303\ 325\ 514\ m/s$$

$$v_{p\_\alpha} = 303\ 326\ \text{km/s}$$

Again, slightly breaking the speed limit. The simulation velocity is very similar, as expected with the same L and C matrices used in both calculation and simulation, since they already create a balanced ZY matrix without alteration:

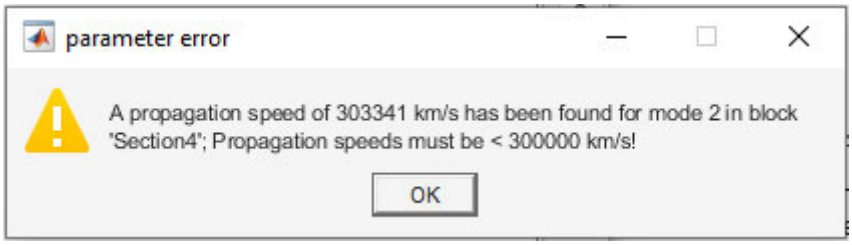

Figure 23. Propagation velocity in the simulated symmetric model.

Again, very close result for manual calculation vs simulation (99.995%). Correlation with previously seen time intervals:

$v_p = d/t$ where d = 800 km

$t = d/v_p$

$t = 800\,000 / 303\,325\,514$

$t = 2.637$ ms

This almost matched the initial open circuit findings from Table 1 (99.96% similar at 3 decimal places). Both the manual calculation and simulation results seemed to correlate that the propagation velocity is slower by 1.1% in the asymmetric model. However, addressing the speed limit problem, the ideal asymmetric model should have an upper limit of ***c***, so the model was overestimating by at least 1.1%. The observed velocity difference between models was within the inherent overestimation error. Therefore, a real difference was so far rejected.

4.5 Zero Sequence Ground Mode

Continuing the attempt to make the peak measurement more robust for non-open circuit fault simulations, zero sequence current ground mode (mode '0') comparison was used. This is expected to be slower than the aerial modes (α & β) calculated above (Chalangar et al. 2019), but if it provided a more confident manual peak measurement, then it can further confirm or reject both the initial variation amongst fault types displayed in Table 1, and the propagation velocity difference between asymmetric vs symmetric model. This method was only applicable to ground faults because 'zero sequence' means the lines are all at the same voltage at any instant, so there won't be a line-line fault:

The following are examples of travelling waves produced by zero sequence current with line-to-ground (L-G) faults:

Asymmetric:

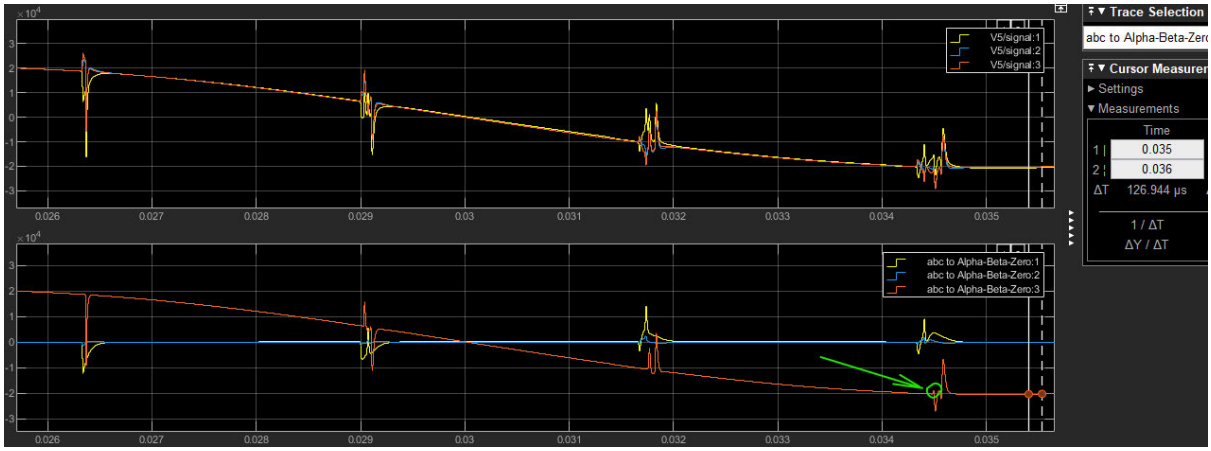

Figure 24. Travelling waveforms for the zero sequence L-G fault on the asymmetric model. The top trace is the 3 phases a, b and c, and the bottom trace is the 3 modes α (yellow), β (blue) and 0 (red), the latter being the focus of interest in this test. Green arrow highlights the beginning of ambiguous peaks.

Symmetric:

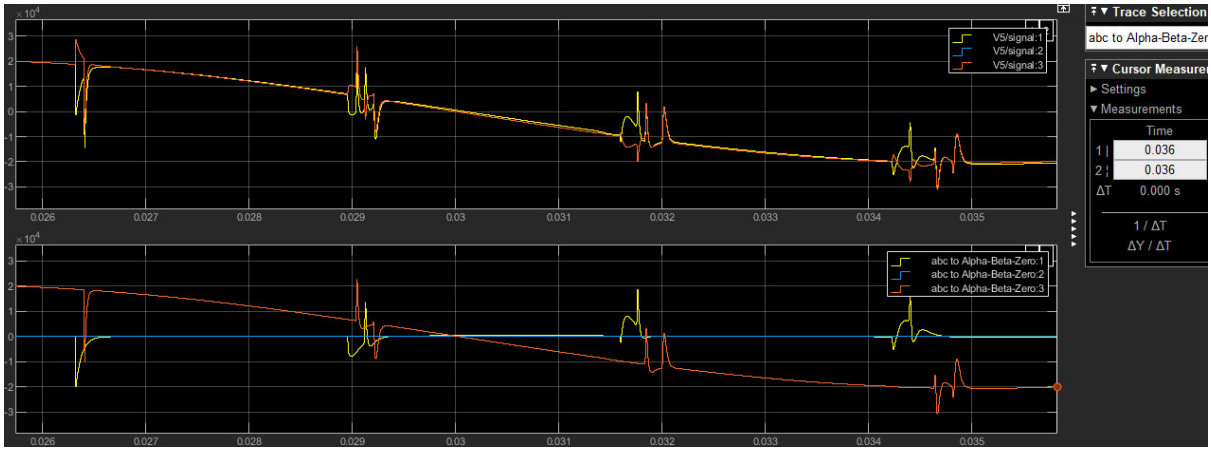

Figure 25. Travelling waveforms for the zero sequence L-G fault on the symmetric model. The top trace is the 3 phases a, b and c, and the bottom trace is the 3 modes α (yellow), β (blue) and 0 (red), the latter being the focus of interest in this test.

Using the ground mode peaks (bottom red trace) in the symmetric model above, the waveforms did seem to have an improved peak clarity compared to the phase peaks (top trace) for at least the first three wave groups. The peaks became ambiguous from the fourth group onwards. The following results (Table 2 over page) were therefore the average of only the first two intervals, unlike the first three intervals represented previously in Table 1.

*Table 2. Average zero sequence ground mode peak intervals for the first three groups of waves, measured for different fault types on both symmetric and asymmetric models. The latter is **not** the zeroth-order (averaged) model.*

	Fault type	Interval between peaks (ms)	
		Symmetric	Asymmetric
Ground Faults	L-G	2.721	2.698
	L-L-G	2.719	2.699
	L-L-L-G	2.804	2.732

The propagation velocity variation was almost equal for L-G compared to L-L-G faults (>99.93% similar, with the difference likely within measurement error), however the L-L-G fault was different (96.97 - 98.79% similar), and therefore slower. This was not seen initially in Table 1. This warrants further investigation, but is outside the scope of this study.

Another striking difference observed in the zero-sequence ground mode results (Table 2) compared to the original phase results (Table 1) is that the asymmetric model presented a *faster* ground mode propagation velocity than the symmetric model (0.85 – 2.6%). Checking back to the manual matrix calculations (page 54), this result was also seen there:

The decoupled modal matrices for the asymmetric and symmetric systems gave λ_0 values of

-0.1150×10^{-11} and -0.1211×10^{-11} respectively.

Using the previous:

$$v_p = \frac{\omega}{\sqrt{\lambda}}$$

The propagation velocity is inversely proportional to λ, so the asymmetric model again generated the larger ground mode propagation velocity by 2.6% (2.9291×10^8 vs 2.8550×10^8 m/s). This difference is outside the inherent model overestimation error (1.1%). This was not an artefact of the averaging method or zero-sequence injection, since the simulation peak measurements (Table 2) are from the non-averaged asymmetric matrices and the mathematical calculation was independent of sequence.

It could yet be concluded that asymmetry caused the different ground mode velocities. The two models are not actually directly comparable in this way, because there are other inherent geometric differences that are likely to have an effect, outside of symmetry. For example, the conductor distances, especially earth-return distance ***D***, are likely factors, and are fundamentally different between the two models. This was investigated next.

4.6 Effect of Conductor Distance *D*

The attempt was made at the beginning to make the phase distances ***x*** as comparable as possible, by using the geometric mean distance of asymmetric model phases as the phase distance in the symmetric model (page 36). However, the earth-return distance ***D*** is vastly different. For example, consider the geometry of the two models below, with the contrasting conductor distances 'D' and 'x':

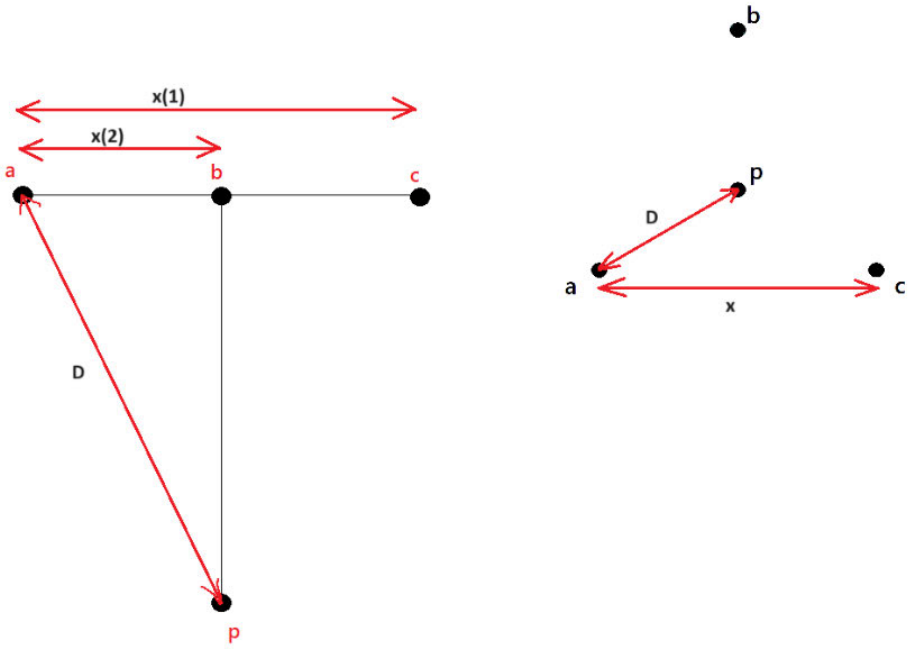

*Figure 26. The geometry of the asymmetric (left) vs symmetric models (right), to highlight the fundamentally different phase **x** and earth-return **D** distances.*

A careful comparison is required between the two models to enable further confirmation or rejection of the initial results thus far. The earth-return distance ***D*** was investigated for its effects on velocity. The investigation again began with a simple single-phase system using classical equations.

4.6.1 Classical Single Phase

Considering the equations introduced previously (page 48), specifically:

$$v_p = \frac{1}{\sqrt{LC}} \quad \text{and} \quad L = 4x10^{-7}\left(\ln\left(\frac{D}{r\prime}\right)\right) \quad \text{and} \quad C = \frac{\pi\varepsilon}{\ln\left(\frac{D}{r}\right)}$$

The inductance and capacitance per unit of the two-wire system are based on the proportion of conductor separation distance to conductor radius, i.e., $\left(\frac{D}{r}\right)$. As conductors are separated (↑D),

inductance increases while capacitance decreases. To explain this in the real world, think of the current direction of a conductor, with its earth-return therefore being the opposite direction. Magnetic field vectors (from inductance) diminish each other if they are created by two opposing current directions. Conversely, electric field gradients (from capacitance) of two opposite charges (+/-) are additive.

The distance between a single phase and its earth-return was quite different in the symmetric and asymmetric models, being very close in the former and relatively far away in the latter (pole height):

The asymmetric system earth-return distance was discussed in section 4.2.1 (page 48). For the *symmetric* system, D = 0.8984 m and gave:

$L = 1.899 \times 10^{-06}$ H/m

$C = 6.184 \times 10^{-12}$ F/m

$v_p = 2.918 \times 10^{8}$ m/s

A similar velocity result was obtained on the simulator (below) with the above L and C parameters:

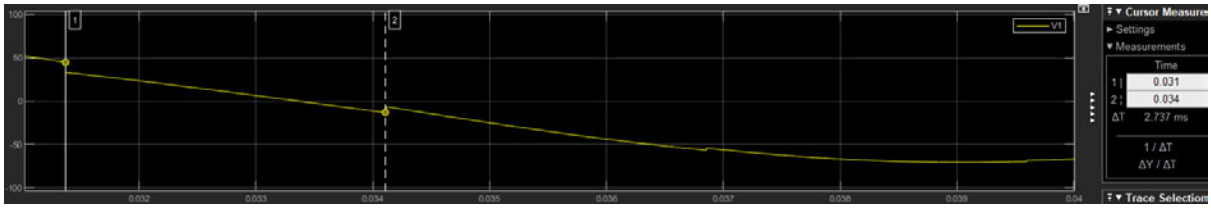

*Figure 27. Single-phase travelling wave peaks for conductor distance **D** used in the symmetric system. The time interval between peaks averaged 2.741 ms, which equates to 2.919 x 10^8 m/s.*

As seen previously for the *asymmetric* system, D = 10.4189 m (the average earth-return distance) and gave:

$L = 2.880 \times 10^{-06}$ H/m

$C = 4.003 \times 10^{-12}$ F/m

Notice the increased inductance and decreased capacitance values with this greater earth-return distance compared to the previous. One increased while the other decreased, but the velocity had also slightly increased by 0.9%:

$v_p = 2.945 \times 10^{8}$ m/s.

This suggested that the further apart the conductors in the two-wire system, the greater the propagation speed:

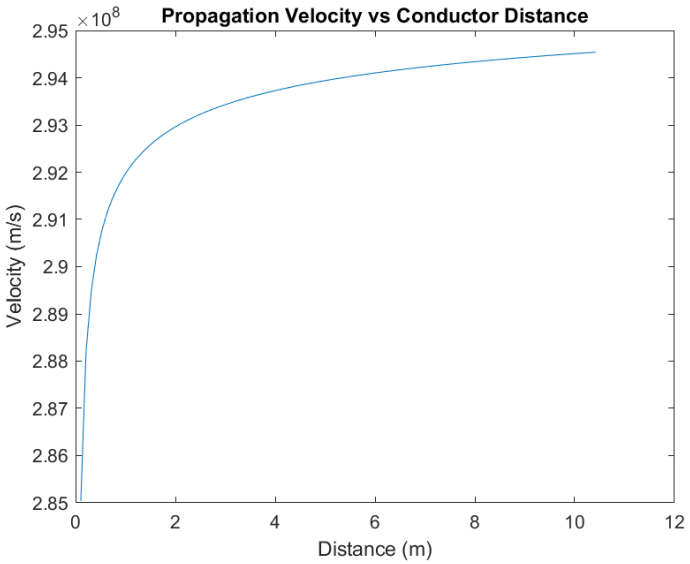

*Figure 28. Propagation velocity calculated from the classical ideal two-wire single phase system equation. It shows that velocity increases with earth-return distance **D** (approaching maximum limit **c**).*

This means that, with increasing earth-return distance, inductance increases at a greater rate than capacitance decreases. The investigation continued with the classical 3-phase system.

4.6.2 Classical 3-Phase

The balanced 3-phase system assumes equal conductor spacing with no neutral or earth currents:

$$L = 2x10^{-7}\left(\ln\left(\frac{D}{r\prime}\right)\right) \qquad \text{and} \qquad C = \frac{2\pi\varepsilon}{\ln\left(\frac{D}{r}\right)}$$

*Note, these are different from the single-phase equations (page 48) by a factor of ½ and 2 respectively.

With the distance used in the *symmetric* system, D = 0.8984 m and gave:

L = 9.496 x 10^{-07} H/m

C = 1.237 x 10^{-11} F/m

v_p = 2.918 x 10^{8} m/s

Note that this is a different L & C to the single-phase result (page 61), but the same resultant velocity.

With the distance used in the *asymmetric* model this time (D = 10.4189 m), the classical 3-phase equations gave:

L = 1.4398 x 10^{-06} H/m

$C = 8.0061 \times 10^{-12}$ F/m

$v_p = 2.945 \times 10^{8}$ m/s.

Again, different L & C as single-phase but same resultant velocity.

The classical single and 3-phase results demonstrated that the distance between phase and earth-return is a critical value. This highlights the care needed when attempting to compare the propagation velocities of symmetric and asymmetric models.

4.6.3 Asymmetric model

To therefore improve comparability between models, the GMD of the asymmetric system earth-return was made to equal the earth-return distance of the symmetric system. This could be akin to adding an actual neutral/ground wire close to the phases of the asymmetric system.

Given D = 0.8984 m for the symmetric, we must make this the GMD of the asymmetric:

$0.8984 = \sqrt[3]{D_{ap}D_{bp}D_{cp}}$ where $D_{ap} = D_{cp}$; and

$D_{bp} = \sqrt{D_{ap}^2 - D_{ab}^2}$ (trigonometric relationship – refer to Figure 7)

Where $D_{ab} = 1.235$ m

$$0.8984^3 = D_{ap}D_{bp}D_{cp}$$

$$0.8984^3 = D_{ap}^2 D_{bp}$$

$$0.8984^3 = D_{ap}^2\sqrt{D_{ap}^2 - D_{ab}^2}$$

$$0.7251 = D_{ap}^2\sqrt{D_{ap}^2 - 1.235^2}$$

$$D_{ap} = 1.3061 \text{ m} = D_{cp}$$

$$D_{bp} = 0.4251\, m$$

This results in the transformed eigenvalue matrix:

$$[T][ZY]_{bal}[T]^{-1} = \begin{bmatrix} -0.1097 & 0 & 0 \\ 0 & -0.1097 & 0 \\ 0 & 0 & -0.1198 \end{bmatrix} x10^{-11}$$

The aerial mode velocity with the new earth-return distance was almost identical to that of the previous earth-return distance, but the ground mode velocity was significantly different:

$v_{p\_\alpha} = 299\,900\,756\ m/s$ (previously 299 806 142, 0.03% different)

$v_{p\_0} = 287\,014\,936\ m/s$ (previously 292 911 590, 2.0% different)

This made sense, considering that the aerial modes don't involve an earth-return (ground), and the ground mode speed being proportional to ***D*** which is consistent with previous sections 0 and 4.6.2 (these are specific modes of propagation here, not the single speed values calculated in the previously mentioned sections).

Therefore, the above results suggested that the earth-return distance had minimal influence on the model comparisons *for aerial mode velocities*. However, since the earth-return distance had an effect on ground-mode velocity, the next logical question was: *did the different earth-return distance of the original geometry (Figure 26) account for the different ground-mode velocities seen previously (Section 4.5)?*

The original ground-mode difference was 2.6%. Changing the earth-return distance of the asymmetric model to match (GMD) that of the symmetric model dropped the asymmetric ground-mode velocity by 2.0%. The difference between the two models was now 0.5%. Therefore, *the non-symmetry-related effect of earth-return distance accounted for the different ground-mode velocities found previously.*

The influence of the variable ***D*** on propagation velocity was investigated above, so the next logical step was to investigate the influence of the other distance variable - phase to phase distance ***x***. Although the distance ***x*** was already made as similar as possible between the two models, they were not the same, so investigating the possible effect on the model comparison was justified.

4.7 Effect of Phase-to-Phase Distance *x*

Comparing the influence of ***x*** between models is again quite difficult. In the previous section, ***D*** could be manipulated independently (for the asymmetric model only). However, increasing ***x*** also causes an increase in ***D***. Therefore, for the following comparisons, the GMD of ***D*** increased proportionally with ***x***, but was kept equal between models (as per the previous section 4.6.3).

Both aerial and ground mode propagation velocities were investigated over a range of phase conductor distances ***x*** for both models:

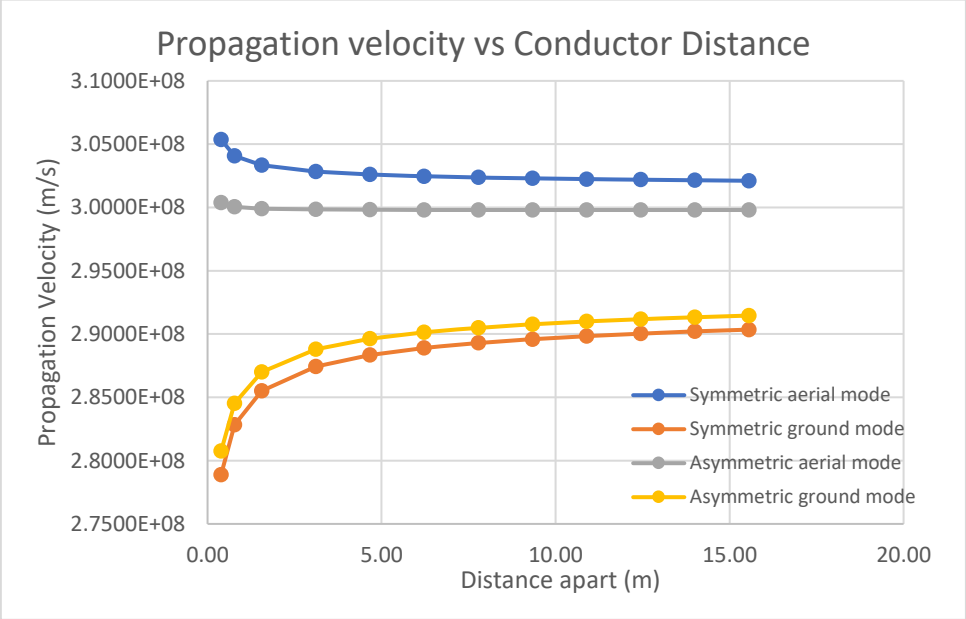

*Figure 29. The effect of phase-to-phase distance **x** on propagation velocity in the asymmetric and symmetric models.*

The aerial and ground mode velocities change over the given range ***x*** (Figure 29 above) in both models. The velocities seem to approach a stable value, in which again the aerial mode is subject to the inherent overestimation error above ***c***. The change in aerial mode velocity with ***x***, from the original distance to the extreme end of the graphs (representing a near stable value), ranges from about 0.6 – 3.9%. However, the trend above shows that this variation will drastically increase as the conductors approach smaller distances (***x***) than shown, which reveals another problem with the models.

It seemed that the inherent error introduced in section 4.4.2 (page 57) also increased drastically as phase distance ***x*** approaches the conductor radius distance (r = 0.01 m). It is likely that this radius distance is the focal point of the problematic assumptions inherent in the model's construction, namely:

- Derivations include conductor internal (x < r) inductance, and therefore an 'equivalent' radius (***r'*** seen in equation 5, page 22), but there's no internal capacitance.
- The internal inductance derivation doesn't account for skin effect: it is essentially applicable as a direct current formula and representative of alternating current.
- The internal inductance also doesn't account for proximity effect which, like skin effect, is likely to influence the internal current and flux distribution.

For further meaningful comparison between models, the inherent assumption issues above need to be addressed. The following was a simple check that the radius distance, subject to the problematic assumptions listed above, was indeed involved in observed errors.

4.8 Model Error and Conductor Radius

The conductor radius (***r***) was originally set to 1 cm. Now the goal was to make it a theoretical 'filament' conductor, which has essentially no radius, minimising the effects of suspected problematic internal inductance calculations. Therefore, internal flux was also discarded from the derivations, since there was now physically no internal component.

The original equations use an equivalent radius to combine both internal and external components. This must now be undone. Mathematically, this involves returning to the standard Equation 5:

$$L_{self} = 4x10^{-7}\left(\ln\left(\frac{D}{r'}\right)\right)$$

By using the equivalent radius ***r'*** to combine both internal and external components, the above equation is actually a simplified form of Equation 6:

$$L_{self} = 4x10^{-7}\left(\frac{1}{4} + \ln\left(\frac{D}{r}\right)\right)$$

where the $\frac{1}{4}$ component in the brackets represents the internal inductance (it is a constant).

Therefore, removing the internal inductance component yields:

$$L_{self} = 4x10^{-7}\left(\ln\left(\frac{D}{r}\right)\right)$$

So, for converting self-inductance equations to self-*external*-inductance equations, the equivalent radius ***r'*** can simply be replaced by actual radius ***r***.

Removing the internal inductance components from the mutual inductance derivations was a similar process. For example, the derivation of inductance from the current in circuit a-p with circuit b-p on page 27 went as follows:

$$L_{ab} = L_{int\,(a)} + L_{int\,(p)} + \left(\frac{\Psi_{ab} + \Psi_{pb}}{I_a}\right)$$

$$L_{ab} = \cancel{0.5x10^{-7}} + \cancel{0.5x10^{-7}} + \frac{\mu_0}{4\pi} \cdot \ln\left(\frac{x^2 + D^2}{x^2 + r^2}\right) + \frac{\mu_0}{2\pi} \cdot \left(\ln\left(\frac{D}{r}\right)\right)$$

Following the process of the page 27 derivation, the internal inductance could be removed from the final equation as follows:

$$L_{ab} = 1x10^{-7}\left(\cancel{1} + \ln\left(\frac{D^2(x^2 + D^2)}{r^2(x^2 + r^2)}\right)\right)$$

To complete the 'filament model', the conductor radius was set to 1 x 10^{-12} m.

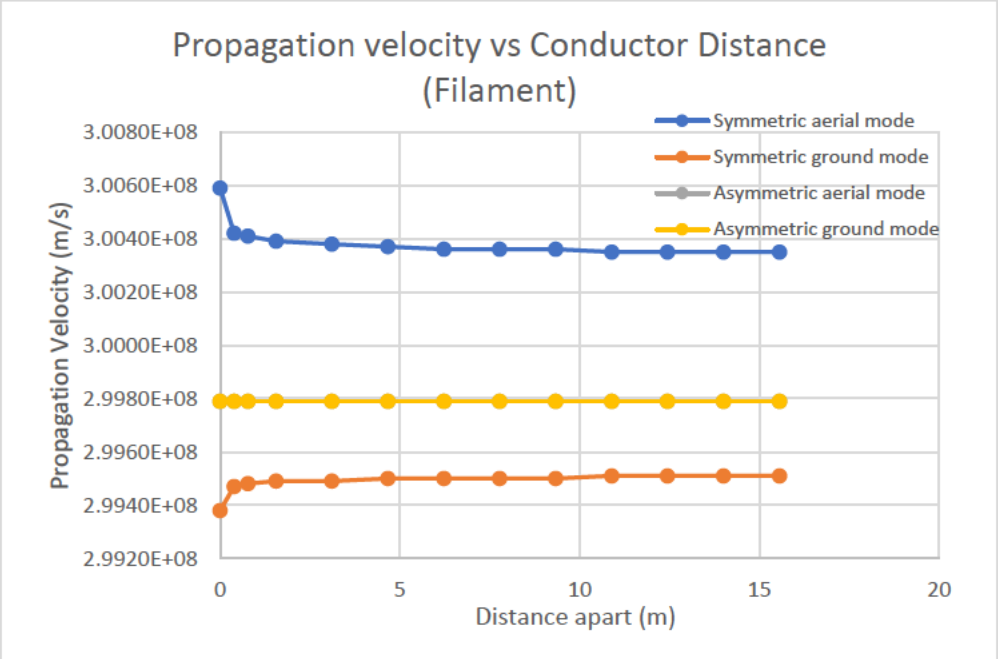

Figure 30. The effect of phase-to-phase distance x on propagation velocity in the asymmetric and symmetric models now with filament conductors. Note that asymmetric aerial (yellow) and ground mode (grey) occupy the same space.

Including a new first point of x = 0.001 m, the trends now showed almost no variation (<0.08%) over the range of x, compared to the previous non-filament conductor results (Figure 29). The asymmetric model had no variation, and the aerial and ground modes were both equal to ***c***. The symmetric model aerial modes were also much closer to each other and to ***c***. The original comparisons, now with the filament conductors, are summarised below:

*Table 3. Propagation velocities for aerial and ground modes on asymmetric and symmetric filament conductor models (original **x** values).*

	Propagation Velocity (m/s)	
Geometry	$v_{p\ \alpha}$	$v_{p\ 0}$
Symmetric	3.0039 x 10^8	2. 9949 x 10^8
Asymmetric Original	2.9979 x 10^8	2.9979 x 10^8
Asymmetric Similar *D*	2.9979 x 10^8	2.9979 x 10^8

The aerial mode velocity of the symmetric model was now only 0.2% above ***c*** compared to the previous 1.1%, suggesting that the overestimation error at least was reduced. This also meant that the difference in velocity displayed by the two models was also only 0.2%, and the asymmetric velocity was at the theoretical maximum.

The conductor radius distance ***r*** was clearly involved in the inherent velocity overestimation, lending weight to the suggested probable causes in the derivation assumptions.

CHAPTER 5

CONCLUSIONS AND RECOMMENDATIONS

5.1 Introduction

The main goal of the present study was to establish the effect of asymmetry on travelling wave propagation velocity. Initial findings from simulated peak measurements indeed suggested a difference between the symmetric and asymmetric model velocities (1.1%). They also suggested a different velocity for different fault types.

This interesting result created an investigative tangent. The fault type differentiation was investigated further with modal peak analysis and analytical investigation. The outcome was that those initial variations were an artefact of measurement error. Interestingly however, the zero-sequence ground mode injection test (Section 4.5) produced a different velocity for the three-phase-to-ground (L-L-L-G) fault than the 1- and 2-phase-to-ground (L-G and L-L-G) faults, which didn't happen with the normal 3-phase source. This warrants further investigation. Outside of this special case however, there was no evidence in this study to suggest any different propagation velocities between fault types with a standard sequence source.

Returning to the main investigation of symmetry effects on velocity, the analytical investigation correlated with the initial simulation measurements, that the symmetric model had a slower aerial mode propagation velocity (1.1%). However, this was within the inherent overestimation error of the model, wherein the symmetric velocity was 1.1% above the expected ideal value $\boldsymbol{c}$.

An interesting result from the modal analysis, both simulation and analytical, was that the ground mode velocity was greater in the asymmetric model than the symmetric (by 2.6%), unlike the aerial propagation modes. This difference could not be accounted for by the inherent model error. However, there are fundamental differences between the two models outside of symmetry, and a direct comparison could not yet be made.

Therefore, the velocity comparability of the two models was investigated. The difference observed, at least in ground mode velocities, led to the question: *could a difference in velocities between the two models be caused by non-symmetry-related parameters such as earth-return distance?* The asymmetric model originally had a much greater earth-return distance than the symmetric. The classical equations demonstrated that this distance was critical, with propagation velocity increasing toward $\boldsymbol{c}$ with conductor separation.

This question was addressed by making the geometries as comparable as possible by using equal geometric mean conductor distances, and investigating the influence of phase-to-phase and earth-return conductor distances on propagation velocity. The results suggested that the earth-return distance had almost no influence on aerial mode propagation velocity (0.03% difference between ground level earth and symmetric-similar earth distance), but had enough influence on ground mode velocity (2.0%) to account for the difference originally observed. Therefore, there was no velocity difference observed outside the inherent model error.

For completeness, the influence of phase-to-phase distance on propagation velocity was investigated also. This led to confronting the model error and the problematic assumptions upon which the models were derived. These were evident initially by producing aerial mode velocities always slightly above $\boldsymbol{c}$, and finally going far above $\boldsymbol{c}$ when conductor distances were reduced toward conductor radial distances.

The main suspected problematic assumption was that frequency, and therefore both skin effect and proximity effect, were not accounted for. They would likely have an influence, especially at high frequencies that are typical of travelling waves (de Magalhães Júnior & Lopes 2021). Therefore, the models probably made an overestimation of inductance and an underestimation of capacitance, but not by the same rate (remembering the propagation velocity calculation is dependent on the product of the two). Hence, a higher than light speed overestimation occurred, increasing with conductor distance.

To conclude, while the model has some inherent error, the results in the present study show no difference in travelling wave propagation velocity between derived symmetrical and asymmetrical models. There is no implication based on symmetry for improving current fault location device accuracy.

5.2 Final Conclusion

Asymmetry has no effect on the propagation velocity of travelling waves.

5.3 Recommendations for Further Work

1. The model has some inherent error. The investigation may be worth continuing with an improved model in which the shortcomings of the present derivation assumptions are corrected.

2. It is suspected that transposition may have been incorporated by the mathematical averaging method of the present study. It is recommended to also test transposition directly on the simulator for verification.

3. There were some interesting ground mode results, such as:
    a. the 3-phase-to-ground fault travelling wave velocity was slower than other fault types when zero sequence current was injected; and
    b. The ground mode and aerial mode velocities were identical on the asymmetric filament model.

    However, the present study models the earth-return as a second identical and ideal conductor, and the above findings may be an artefact of this. It is recommended to investigate further with an improved model that includes a more realistic earth-return path. The literature reports that the ground mode propagation is slower (Chalangar et al. 2019). This is likely due to the different material properties of the earth compared to a transmission line, specifically, the permittivity. For example, equation 31:

$$C = \frac{\pi\varepsilon}{\ln\left(\frac{D}{r}\right)} \qquad \text{F/m}$$

    Permittivity is directly proportional to capacitance, and therefore inversely proportional to propagation velocity. The present model uses the ideal (vacuum) minimum relative permittivity ($\varepsilon = \varepsilon_0 = 1$). This yields the fastest travelling wave. Cables generally have a permittivity below 10 (IEC 2014). The earth permittivity is generally much higher and greatly affected by water content (Owenier, Hornung & Hinderer 2018), which has a relative permittivity of 80 (Thring et al. 2014), resulting in a slower ground mode propagation. Incorporating this into the model would enable a much more capable further investigation of the ground mode results in this study.

REFERENCES

Ancell, G & Pahalawaththa, N 1994, 'Maximum likelihood estimation of fault location on transmission lines using travelling waves', *IEEE Transactions on Power Delivery*, vol. 9, no. 2, pp. 680-9.

Bellan, D 2019, 'Analytical approach to transient solution of single-line and double-line faults in three-phase circuits', *International Journal of Circuits, Systems and Signal Processing*, vol. 13, pp. 647-53.

Bellan, D 2020, 'Clarke Transformation Solution of Asymmetrical Transients in Three-Phase Circuits', *Energies*, vol. 13, no. 19.

Bellan, D & Superti-Furga, G 2018, 'Space-vector state-equation analysis of three-phase transients', *Journal of Electrical Systems*, vol. 14, no. 1, pp. 188-98.

Carvalho, CGd, Costa, ECM, Kurokawa, S & Pissolato, J 2016, 'Alternative phase-domain model for multi-conductor transmission lines using two modal transformation matrices', *Electric Power Components and Systems*, vol. 44, no. 3, pp. 291-301.

Chalangar, H, Ould-Bachir, T, Sheshyekani, K, Li, S & Mahseredjian, J 2019, 'Evaluation of a constant parameter line-based TWFL real-time testbed', *IEEE Transactions on Power Delivery*, vol. 35, no. 2, pp. 1010-9.

Da Costa, ECM, Kurokawa, S, do Prado, AJ & Pissolato, J 2011, 'Proposal of an alternative transmission line model for symmetrical and asymmetrical configurations', *International Journal of Electrical Power & Energy Systems*, vol. 33, no. 8, pp. 1375-83.

Das, S, Santoso, S, Gaikwad, A & Patel, M 2014, 'Impedance-based fault location in transmission networks: theory and application', *IEEE access*, vol. 2, pp. 537-57.

de Magalhães Júnior, FM & Lopes, FV 2021, 'Mathematical Study on Traveling Waves Phenomena on Three Phase Transmission Lines–Part I: Fault-Launched Waves', *IEEE Transactions on Power Delivery*, vol. 37, no. 2, pp. 1151-60.

ENTSO-E 2021, *Use of Travelling Waves Principle in Protection Systems and Related Automations.*, European Network of Transmission System Operators for Electricity, chrome-extension://efaidnbmnnnibpcajpcglclefindmkaj/https://eepublicdownloads.entsoe.eu/clean-

documents/SOC%20documents/USE_OF_TRAVELLING_WAVES_PRINCIPLE_IN_PROTECTION_SYSTEMS_AND_RELATED_AUTOMATIONS.pdf>.

Faria, JB 2000, 'Application of clarke's transformation to the modal analysis of asymmetrical single-circuit three-phase line configurations', *European transactions on electrical power*, vol. 10, no. 4, pp. 225-31.

Faria, JB & Briceno, JH 1997, 'On the modal analysis of asymmetrical three-phase transmission lines using standard transformation matrices', *IEEE Transactions on Power Delivery*, vol. 12, no. 4, pp. 1760-5.

Faria, JB & Mendez, JB 1997, 'Modal analysis of untransposed bilateral three-phase lines-a perturbation approach', *IEEE Transactions on Power Delivery*, vol. 12, no. 1, pp. 497-504.

Guzmán, A, Kasztenny, B, Tong, Y & Mynam, MV 2018, 'Accurate and economical traveling-wave fault locating without communications', *2018 71st Annual Conference for Protective Relay Engineers (CPRE)*, IEEE, pp. 1-18.

Hedman, D 1965, 'Propagation on overhead transmission lines I-Theory of modal analysis', *IEEE Transactions on Power Apparatus and Systems*, vol. 84, no. 3, pp. 200-5.

IEC 2014, *60287-1-1*, Electric cables - Calculation of the current rating - Part 1-1: Current rating equations (100 % load factor) and calculation of losses - General.

IEEE 2014, *IEEE Guide for Determining Fault Location on AC Transmission and Distribution Lines*, IEEE Std C37.114-2014 (Revision of IEEE Std C37.114-2004).

Kaloudas, CG, Papadopoulos, T & Papagiannis, G 2008, 'Transient Performance of Overhead Transmission Lines above Stratified Earth of Varying Permittivity', *Proceedings of the*.

Krzysztof, G, Kowalik, R & Rasolomampionona, D 2011, 'Travelling Wave Fault Location In Power Transmission Systems: An Overview', *J. electrical Systems*, vol. 7, no. 3, pp. 287-96.

Liang, R, Yang, Z, Peng, N, Liu, C & Zare, F 2017, 'Asynchronous fault location in transmission lines considering accurate variation of the ground-mode traveling wave velocity', *Energies*, vol. 10, no. 12, p. 1957.

Lu, D, Liu, Y, Huang, W & Xi, X 2020, 'Accurate fault location in AC/DC hybrid line corridors based on eigenvalue decomposition', *2020 IEEE Power & Energy Society General Meeting (PESGM)*, IEEE, pp. 1-5.

Lu, D, Liu, Y, Wang, B, Yi, L & Zheng, X 2021, 'Accurate Time-Domain Fault Location Method on Practically Transposed Transmission Lines', *2021 IEEE Power & Energy Society General Meeting (PESGM)*, IEEE, pp. 1-5.

Mamiş, M & Nacaroğlu, A 2002, 'Transient voltage and current distributions on transmission lines', *IEE Proceedings-Generation, Transmission and Distribution*, vol. 149, no. 6, pp. 705-12.

O'brien, W & Udren, EA 2018, *System for detecting a falling electric power conductor and related methods*, Google Patents.

O'Brien, W, Udren, E, Garg, K, Haes, D & Sridharan, B 2016, 'Catching falling conductors in midair—detecting and tripping broken distribution circuit conductors at protection speeds', *2016 69th Annual Conference for Protective Relay Engineers (CPRE)*, IEEE, pp. 1-11.

Owenier, F, Hornung, J & Hinderer, M 2018, 'Substrate-sensitive relationships of dielectric permittivity and water content: implications for moisture sounding', *Near Surface Geophysics*, vol. 16, no. 2, pp. 128-52.

Pang, S, Tan, F, Zhao, H, Zhang, M, Liao, J & Peng, Y 2019, 'Transmission Attenuation of 110kv Asymmetric Transmission Lines Based on Measured Data', *IOP Conference Series: Materials Science and Engineering*, IOP Publishing, p. 012125.

Prado, A, Kurokawa, S, Pissolato Filho, J & Bovolato, LF 2010, 'Step by step analyses of Clarke's matrix correction procedure for untransposed three-phase transmission line cases', *IEEE PES General Meeting*, IEEE, pp. 1-9.

Prado, A, Kurokawa, S, Bovolato, L & Pissolato Filho, J 2011, 'Corrected phase-mode transformation matrices for three-phase transmission line transient simulations–time domain analyses', *THE 9th LATIN-AMERICAN CONGRESS ON ELECTRICITY GENERATION AND TRANSMISSION*.

Prado, A, Kurokawa, S, Costa, E, Pissolato Filho, J & Bovolato, L 2012, 'Time domain analyses for three-phase lines with corrected modal transformation matrix', *2012 IEEE Power and Energy Society General Meeting*, IEEE, pp. 1-6.

Schweitzer, EO, Guzmán, A, Mynam, MV, Skendzic, V, Kasztenny, B & Marx, S 2014, 'Locating faults by the traveling waves they launch', *2014 67th annual conference for protective relay engineers*, IEEE, pp. 95-110.

Stevenson Jr, W & Grainger, J 1994, *Power system analysis*, McGraw-Hill Education.

Thring, L, Boddice, D, Metje, N, Curioni, G, Chapman, D & Pring, L 2014, 'Factors affecting soil permittivity and proposals to obtain gravimetric water content from time domain reflectometry measurements', *Canadian Geotechnical Journal*, vol. 51, no. 11, pp. 1303-17.

Zhou, B, Zhang, K, Li, Y, Yang, L & Ni, J 2021, 'Study on Measurement Error of Power Frequency Electric Field Intensity Caused by Change of Air Dielectric Constant with Humidity', *IOP Conference Series: Earth and Environmental Science*, IOP Publishing, p. 012022.

APPENDIX

ENG4111/4112 Research Project

Project Specification

For: Rory Taylor

Title: The Effects of Three Phase Asymmetry on Transmission Line Travelling Waves.

Major: Power Engineering

Supervisors: Assoc. Prof. Tony Ahfock

Enrolment: ENG4111 – EXT S1, 2023

ENG4112 – EXT S2, 2023

Project Aim: To investigate the inclusion of losses, arising from 3-phase asymmetry of line arrangement, into the standard velocity equations.

Programme: Version 1, 21st March 2023

1. Research travelling wave and transmission line mathematical theory.
2. Create mathematical models of travelling waves that incorporates asymmetry-related transmission line losses.
3. Incorporate these into Simscape models.
4. Compare and discuss implications of model outcomes for protection systems based on travelling waves.